A general multi-scale topology optimisation method for lightweight lattice structures obtained through additive manufacturing technology

Marco Montemurro, G. Bertolino, T. Roiné

Version of Record: https://www.sciencedirect.com/science/article/pii/S0263822320332864
Manuscript_3cbb26199a53c79e7bdf395e4e9561b6

A General Multi-Scale Topology Optimisation Method for Lightweight Lattice Structures Obtained through Additive Manufacturing Technology

M. Montemurro[a,*], G. Bertolino[a], T. Roiné[a,b]

[a] *Arts et Métiers Institute of Technology, Université de Bordeaux, CNRS, INRA, Bordeaux INP, HESAM Université, I2M UMR 5295, F-33405 Talence, France*
[b] *SEIV Alcen, 10 rue des Bacaris, 33700 MERIGNAC*

Abstract

A general framework for the multi-scale topology optimisation (TO) of lattice structures (LSs) is presented in this work. The proposed method involves: Non-Uniform Rational Basis Spline (NURBS) hyper-surfaces to represent the pseudo-density field describing the LS representative volume element (RVE) topology, the Solid Isotropic Material with Penalisation (SIMP) approach and the strain energy-based homogenisation method (SEHM) to perform the scale transition. The main contributions of this work are essentially three. Firstly, physical responses are defined at different scales and their gradient is evaluated by exploiting the NURBS local support property and the Dirichlet's problem properties at the RVE scale. Secondly, the computational efficiency of the SEHM based on elements strain energy over that of the SEHM based on elements averaged stresses is rigorously proven. Finally, to show the effectiveness of the method, numerical analyses are conducted on 2D and 3D problems. A sensitivity analysis of the optimised topology to the integer parameters of the NURBS hyper-surface is carried out. Moreover, the influence of the initial guess and of the macroscopic loading condition on the RVE optimised topology is investigated. The minimum length-scale requirement is also integrated into the problem formulation as a manufacturing constraint.

Keywords: Topology Optimisation, NURBS Hyper-Surfaces, Lattice Structures, Homogenisation, Additive Manufacturing, Finite Element Method.

1. Introduction

Multi-functional lattice structures (LSs) are of great interest in different engineering fields, like aerospace, automotive and biomedical industries or in the energetic and chemical fields, due to the possibility of designing the material architecture at different scales. In this way it is possible to obtain very specific properties and performances according to the requirements of the problem at hand, e.g. high stiffness-to-weight and strength-to-weight ratii, high permeability, energy absorption and thermal insulation. Nowadays, an increasing amount of research works is devoted to the development of multi-scale design approaches for LSs. The goal is to develop a general design approach by reducing the number of (unnecessary) simplifying hypotheses and by integrating into the problem formulation the design variables involved at different scales. The design variables can be

*Corresponding author. Tel.: +33 55 68 45 422, Fax.: +33 54 00 06 964.
Email address: marco.montemurro@ensam.eu, marco.montemurro@u-bordeaux.fr (M. Montemurro)

either the parameters describing the structure topology at the macroscopic scale or those describing the Representative Volume Element (RVE) topology of the LS at the lower scale (i.e. mesoscopic or microscopic scale depending on the problem characteristic size).

Topology optimisation (TO) is, certainly, one of the most promising methods to perform multi-scale optimisation of LSs. A rather complete state of the art about the design methodologies of LSs and of multifunctional metamaterials can be found in [1, 2]. Indeed, thanks to TO, it is possible to add more freedom in the design process without using predefined RVE configurations [3–9]. The idea at the basis of the TO is that the material is iteratively removed from the design domain and redistributed in order to minimise a prescribed merit function by satisfying the set of imposed design requirements.

In the last three decades, many efforts have been devoted to the development of suitable algorithms for TO. Since the seminal works making use of the so-called homogenisation method [10–12] for shape optimization problems in structural mechanics, important steps forwards have been done. For instance, the Evolutionary Structural Optimisation (ESO) method is based on the combination of a metaheuristic algorithm and the Finite Element (FE) method was introduced in [13]. An extension of the ESO method is the well-known Bi-directional Evolutionary Structural Optimisation (BESO) [14]. Later, the BESO approach has been reformulated in [15, 16], by adding features to obtain mesh-independent results, without checker-board pattern and by introducing a sensitivity number averaging method to speed up convergence. Recently, new evolutionary-based procedures for TO have been developed in the framework of the level-set method (LSM) to obtain smooth topology boundary [17]. In the LSM background, the FE model is used only to evaluate the physical responses involved into the problem formulation. The topology is represented through a level-set function (LSF), whose sign can be conventionally associated to solid or void zones, whereas the zero-level describes the structure boundary [18]. A detailed discussion of the LSM for TO is available in [19]. Often, the LSF is parametrised on the design domain by using dedicated *basis functions*, like Radial Basis Functions, Spectral Parametrization Functions and Non-Uniform Rational Basis Spline (NURBS) entities. A wide discussion on this topic can be found in [20].

Nevertheless, due to their efficiency and robustness, TO algorithms based on a pseudo-density field to describe the structure topology [10, 21, 22] constitute the most widespread technique in both scientific and industrial communities. In a TO algorithm based on a pseudo-density field, the structure topology is described on the basis of a FE mesh, which provide a suitable discretisation of the continuum: a fictitious density function, which takes values in the interval $[0, 1]$, is then affected (through a pertinent penalty scheme) to the characteristic tensors of each element describing the physical phenomena of the problem at hand, e.g. elasticity tensor for structural mechanics, conductivity tensor for thermal problems, etc. Lower and upper bounds of the density function correspond to "void" and "solid" phases, respectively. Inasmuch as a physically meaningful, solid-void design is sought, "gray" elements, characterised by intermediate values of the density function, are allowed but penalised during optimisation. The physical properties of each element are computed (and penalised) according to the local pseudo-density value. The Solid Isotropic Material with Penalisation (SIMP) scheme is the most widespread penalty approach used for TO [21]. The success of the SIMP method is due to its efficiency and compactness [22]: several applications of this method can be found [21].

As far as the strategies dedicated to the multi-scale design of LSs and of metamaterials are concerned, different multi-scale TO methods are available in the literature. They are based on (a) the homogenisation method [23, 24], (b) the LSM [25–30], (c) the SIMP approach [31–35] or (d) the BESO method [36]. These strategies are often applied at the

scale of the LS RVE, in order to find the optimal topology satisfying the requirements of the problem at hand. Typical design requirements are RVE stiffness and relative density [37], RVE shear stiffness [38], or specific conditions related to auxetic LSs [39, 40].

For example, Gao *et al.* [27] make use of the LSM to determine the optimal topology of the LS RVE maximising the bulk modulus and the shear modulus subject to constraints on the volume of the RVE. Conversely, Guest and Prévost [31] adopt a different approach in order to maximise the effective elastic stiffness and the fluid permeability of LSs. The TO problem is formulated in the SIMP framework and the homogenisation is performed numerically using the FE method, by enforcing periodic boundary conditions (PBCs) on the RVE.

In [35], the TO of the RVE of metamaterials with extreme properties subject to a single constraint on the material volume fraction is carried out. The merit function includes requirements on the components of the equivalent elasticity tensor of the homogenised material at the macroscopic scale, like prescribed values of the bulk modulus, of the shear modulus and of the Poisson's ratio. The TO is conducted in the SIMP framework.

In [41], the lattice infill technique (LIT) is used to post-process the optimised topologies provided by the SIMP approach. In this background, the optimal pseudo-density field resulting from the SIMP method, which describes the distribution of the equivalent homogeneous material at the macroscopic scale, is replaced by a LS (of a given topology) characterised by a variable relative density, which matches, locally, the optimal pseudo-density field. The LIT is based on a predefined surrogate mechanical model of the lattice material, trained via LS unit sampling and polynomial curve fitting.

When dealing with multi-scale TO problems, a fundamental step is the homogenisation method, which represents the link between the problem scales. Thanks to the homogenisation phase, the real LS can be replaced by an equivalent homogeneous anisotropic medium at the macroscopic scale. Of course, the homogenisation technique can be applied only if (a) the RVE has a periodic distribution within the structure domain and (b) scales separation occurs.

In the majority of the existing works, the asymptotic homogenisation method (AHM) is used to perform the scale transition. For example, in [42], the equivalent elastic properties of the LS at the macroscopic scale are computed by using an approximation of the displacement field via Taylor expansion. Similarly, in [39, 43, 44] the AHM is coupled to the Isogeometric analysis (IGA), wherein the physical fields are evaluated by means of Basis Spline (B-spline) entities and where the boundary conditions (BCs) can be applied directly to the control points (CPs) of the B-spline entity.

A different homogenisation scheme is the so-called strain energy-based homogenisation method (SEHM), which is exploited in different works [27, 31, 34, 35, 38, 45]. It represents a sound alternative to the AHM, due to its straightforward numerical implementation and direct coupling with the SIMP approach. The SEHM is based on the equivalence between the strain energy of the heterogeneous LS RVE and that of the corresponding volume of the equivalent homogenised anisotropic medium. The difference between the variants of the SEHM available in the literature is in the post-processing of the outcomes of the SEHM to assess the macroscopic elasticity tensor of the LS. Indeed, one can retrieve either the averaged elements stresses inside the RVE [31] (in this case the resulting homogenisation scheme is called volume-averaged stress-based SEHM) or the elements strain energy [27].

As it can be inferred from this non-exhaustive literature survey, current multi-scale TO approaches for LSs suffer from three main limitations. The first one is related to the problem formulation, which often includes only requirements on prescribed values of the macroscopic elastic tensor components of the LS as done in [25–27, 30, 31, 33–40, 46].

However, in real-world engineering applications the RVE topology at the lower scale must be optimised in order to satisfy design requirements on macroscopic structural responses, like compliance, mass, strength, etc.
The second one is related to the choice of the homogenisation scheme establishing the link between the problem scales. The homogenisation procedure must be as general as possible to avoid the introduction of unnecessary simplifying hypotheses. Moreover, it must be efficient to reduce the computational time for assessing the macroscopic elasticity tensor of the LS, as well as the gradient of the macroscopic responses with respect to the topological variable defined at the lower scale.
The third limitation is related to the integration of suitable manufacturing constraints of geometrical nature in the problem formulation. For instance, the minimum length scale requirement should be considered in order to ensure that small topological branches could be manufactured by means of the considered process.

The above aspects have been addressed in this study. The proposed multi-scale TO approach makes use of: (a) the SIMP method reformulated in the framework of the NURBS hyper-surfaces [47, 48] and (b) the SEHM to set the link between the problem scales. Unlike the classical SIMP approach, the NURBS-based SIMP method separates the pseudo-density field, describing the topology of the continuum, from the mesh of the FE model. More precisely, for general 3D TO problems, a 4D NURBS hyper-surface is used as a topology descriptor, whilst for 2D problems a standard 3D NURBS surface is employed. In this way, the topology descriptor relies on a purely CAD-compatible geometric entity. Moreover, during the FE analysis the NURBS hyper-surface describing the pseudo-density field is projected on the mesh of the FE model in order to penalise the element stiffness matrix according to the SIMP method. In this background, the optimisation variables are the density at each CP and the associated weight. In the framework of the NURBS-based SIMP method, the CAD reconstruction phase becomes a trivial task [47, 48]. Moreover, thanks to the remarkable properties of the NURBS basis functions, the design requirements are satisfied on the reassembled optimised geometry [49, 50]. As discussed in [51, 52], NURBS entities allow for handling in the most efficient way the design requirements of geometrical nature during the optimisation process.

Furthermore, in this study the following question has been addressed: what is the most efficient (in terms of computational costs) variant of the SEHM approach when coupled to a TO algorithm? In particular, a rigorous proof about the computational efficiency of the SEHM based on the elements strain energy when compared to the SEHM based on elements averaged stresses is provided. Moreover, the Dirichlet's problem properties together with the geometrical properties of the NURBS entities are exploited in deriving the analytical expression of the gradient of the macroscopic physical responses with respect to the topological variable defined at the RVE scale. To this end, the analytical formula of the gradient of the macroscopic requirements takes advantage from the local support property of the NURBS blending functions [53], which establishes an implicit relationship among the pseudo-densities of adjacent elements. Thanks to this property there is no need of introducing complicated filtering schemes, unlike the classical SIMP method. The effectiveness of the proposed approach is tested on 2D and 3D benchmark problems. In this background, a sensitivity analysis of the optimised topology to the integer parameters, involved in the definition of the NURBS hyper-surface, is carried out. Moreover, the influence of the initial guess and of the macroscopic loading condition on the optimised topology of the RVE is also investigated.

The paper is articulated as follows. In Section 2, the theoretical background of NURBS hyper-surfaces is briey recalled. The fundamentals of the SEHM are briefly recalled in

Section 3, while the formulation of the multi-scale TO problem in the NURBS-based SIMP framework is presented in Section 4. The numerical results on 2D and 3D test cases are illustrated in Section 5. Finally, Section 6 ends the paper with some conclusions and prospects.

Notation. Upper-case bold letters are used to indicate tensors and matrices, while lower-case bold letters indicate column vectors. $\sharp\mathbf{v}$ denotes the cardinality of the generic vector $\mathbf{v}$, while superscripts m and M denote quantities evaluated at RVE and macroscopic scales, respectively.

2. NURBS hyper-surfaces

A NURBS hyper-surface is a polynomial-based function, defined over a *parametric space* (domain), taking values in the *NURBS space* (co-domain). Therefore, if N is the dimension of the *parametric space* and M is the dimension of the *NURBS space*, a NURBS entity is defined as $\mathbf{h} : \mathbb{R}^N \longrightarrow \mathbb{R}^M$. The mathematical formula of a generic NURBS hyper-surface is

$$\mathbf{h}(u_1, \ldots, u_N) = \sum_{i_1=0}^{n_1} \cdots \sum_{i_N=0}^{n_N} R_{i_1,\ldots,i_N}(\zeta_1, \ldots, \zeta_N)\mathbf{P}_{i_1,\ldots,i_N}, \tag{1}$$

where $R_{i_1,\ldots,i_N}(\zeta_1, \ldots, \zeta_N)$ are the piece-wise rational basis functions, which are related to the standard NURBS blending functions $N_{i_k,p_k}(\zeta_k)$, $k = 1, \ldots, N$ by means of the relationship

$$R_{i_1,\ldots,i_N} = \frac{\omega_{i_1,\ldots,i_N} \prod_{k=1}^{N} N_{i_k,p_k}(\zeta_k)}{\sum_{j1=0}^{n_1} \cdots \sum_{j_N=0}^{n_N} \left[\omega_{j_1,\ldots,j_N} \prod_{k=1}^{N} N_{j_k,p_k}(\zeta_k)\right]}. \tag{2}$$

In Eqs. (1) and (2) , $\mathbf{h}(\zeta_1, \ldots, \zeta_N)$ is a M-dimension vector-valued rational function, ζ_k is the k-th dimensionless coordinate (or parametric coordinate) defined in the interval $[0, 1]$, whilst $\mathbf{P}_{i_1,\ldots,i_N}$ are the CPs. The j-th CP coordinate $(X^{(j)}_{i_1,\ldots,i_N})$ is stored in the array $\mathbf{X}^{(j)} \in \mathbb{R}^{(n_1+1)\times\cdots\times(n_N+1)}$. The explicit expression of CPs coordinates in $\mathbb{R}^M$ is:

$$\begin{aligned} \mathbf{P}_{i_1,\ldots,i_N} &= \{X^{(1)}_{i_1,\ldots,i_N}, \ldots, X^{(M)}_{i_1,\ldots,i_N}\}, \\ \mathbf{X}^{(j)} &\in \mathbb{R}^{(n_1+1)\times\cdots\times(n_N+1)},\ j = 1, \ldots, M. \end{aligned} \tag{3}$$

Curves and surfaces formulæ can be easily deduced from Eq. (1). For example, one scalar parameter ($N = 1$) can describe both a plane curve ($M = 2$) and a 3D curve ($M = 3$). In the case of a surface, two scalar parameters are needed ($N = 2$) together with, of course, three coordinates $M = 3$. Furthermore, for NURBS surfaces, $\mathbf{P}^{\mathrm{T}}_{i_1,i_2} = \{X^{(1)}_{i_1,i_2}, X^{(2)}_{i_1,i_2}, X^{(3)}_{i_1,i_2}\}$ and each coordinate is arranged in a matrix defined in $\mathbb{R}^{(n_1+1)\times(n_2+1)}$. The CPs layout is referred as *control polygon* for NURBS curves, *control net* for surfaces and *control hyper-net* otherwise [53]. The generic CP does not actually belong to the NURBS entity but it affects its shape by means of its coordinates. A weight $\omega_{i_1,\ldots,i_N}$ is associated to the generic CP. The higher the weight $\omega_{i_1,\ldots,i_N}$, the more the NURBS entity is attracted towards

the CP $\mathbf{P}_{i_1,\ldots,i_N}$. For each parametric direction ζ_k, $k = 1,\ldots,N$, the NURBS blending functions are of degree p_k and can be defined in a recursive way as

$$N_{i_k,0}(\zeta_k) = \begin{cases} 1, \text{ if } v_{i_k}^{(k)} \leq \zeta_k < v_{i_k+1}^{(k)}, \\ 0, \text{ otherwise,} \end{cases} \tag{4}$$

$$N_{i_k,q}(\zeta_k) = \frac{\zeta_k - v_{i_k}^{(k)}}{v_{i_k+q}^{(k)} - v_{i_k}^{(k)}} N_{i_k,q-1}(\zeta_k) + \frac{v_{i_k+q+1}^{(k)} - \zeta_k}{v_{i_k+q+1}^{(k)} - v_{i_k+1}^{(k)}} N_{i_k+1,q-1}(\zeta_k), \quad q = 1, ..., p_k, \tag{5}$$

where each constitutive blending function is defined on the knot vector

$$\mathbf{v}_{(k)}{}^{\mathrm{T}} = \{\underbrace{0,\ldots,0}_{p_k+1}, v_{p_k+1}^{(k)}, \ldots, v_{m_k-p_k-1}^{(k)}, \underbrace{1,\ldots,1}_{p_k+1}\}, \tag{6}$$

whose dimension is $m_k + 1$, with

$$m_k = n_k + p_k + 1. \tag{7}$$

Each knot vector $\mathbf{v}_{(k)}$ is a non-decreasing sequence of real numbers that can be interpreted as a discrete collection of values of the related dimensionless parameter ζ_k. The NURBS blending functions are characterised by several interesting properties: the interested reader is addressed to [53] for a deeper insight into the matter. Here, only the *local support property* is recalled because it is of paramount importance for the NURBS-based SIMP method for TO [47, 48]:

$$\begin{aligned} &R_{i_1,\ldots,i_N}(\zeta_1,\ldots,\zeta_N) \neq 0, \\ &\text{if } (\zeta_1,\ldots,\zeta_N) \in \left[v_{i_1}^{(1)}, v_{i_1+p_1+1}^{(1)}\right[\times \cdots \times \left[v_{i_N}^{(N)}, v_{i_N+p_N+1}^{(N)}\right[. \end{aligned} \tag{8}$$

Eq. (8) means that each CP (and the respective weight) affects only a precise zone of the *parametric space*, which is denoted as *local support*.

3. The strain energy homogenisation method

At the mesoscopic scale, the RVE of the LS can be interpreted, from a mechanical point of view, as an heterogeneous medium composed of two phases, i.e. the bulk material and the void. Conversely, at the macroscopic scale it can be modelled as an equivalent homogeneous anisotropic continuum whose mechanical response is described by a set of *effective* (or equivalent) material properties.

This work focuses only of the elastic behaviour of the LS at the macroscopic scale, thus, the macroscopic elasticity tensor (represented as a matrix $\mathbf{C}^M \in \mathbb{R}^{6\times6}$ through the Voigt's notation) of the LS is determined by means of the SEHM. This technique makes use of the repetitive unit of the periodic structure to evaluate the resulting properties at the macroscopic scale. The basic assumption of the SEHM is that the strain energy of the RVE is equal to the counterpart of the corresponding "envelope volume" of the homogeneous anisotropic medium replacing the LS at the macroscopic scale. This homogenisation scheme has proven to be an efficient numerical procedure able to determine the equivalent properties of different heterogeneous materials characterised by complex RVE topologies

[54, 55].
In order to evaluate $\mathbf{C}^M$, three further hypotheses have to be considered: (a) the bulk material of the LS is characterised by a linear, elastic behaviour; (b) small displacements and strains occurs when the RVE is subject to given BCs; (c) the buckling of the RVE thin topological branches (that could appear during the optimisation process) is neglected.

To assess the components of $\mathbf{C}^M$, the RVE is submitted to a uniform strain field $\varepsilon^m_{ij,0}$, with $i,j = 1,2,3$ (tensor notation). The six independent components of the strain tensor are applied one at time by considering the following set of PBCs [56]:

$$\begin{aligned} u_i^m(a_1^m, x_2^m, x_3^m) - u_i(-a_1^m, x_2^m, x_3^m) &= 2a_1^m \varepsilon^m_{i1,0}, \\ u_i^m(x_1^m, a_2^m, x_3^m) - u_i^m(x_1^m, -a_2^m, x_3^m) &= 2a_2^m \varepsilon^m_{i2,0}, \\ u_i^m(x_1^m, x_2^m, a_3^m) - u_i^m(x_1^m, x_2^m, -a_3^m) &= 2a_3^m \varepsilon^m_{i3,0}, \\ \forall x_i^m \in [-a_i^m, a_i^m],\ i &= 1,2,3. \end{aligned} \tag{9}$$

In the above formula, a_i^m is the characteristic length of the RVE along the x_i^m axis, while u_i^m is the component of the displacement field along the same axis. Consider now the equilibrium equation of the FE model of the RVE. In the most general case it reads:

$$\hat{\mathbf{K}}^m \hat{\mathbf{u}}^m = \hat{\mathbf{f}}^m; \quad \hat{\mathbf{u}}^m, \hat{\mathbf{f}}^m \in \mathbb{R}^{\hat{N}^m_{\mathrm{DOF}}},\ \hat{\mathbf{K}}^m \in \mathbb{R}^{\hat{N}^m_{\mathrm{DOF}} \times \hat{N}^m_{\mathrm{DOF}}}, \tag{10}$$

where $\hat{N}^m_{\mathrm{DOF}}$ is the overall number of degrees of freedom (DOFs) of the structure before the application of the BCs, while $\hat{\mathbf{K}}^m$ is the non-reduced (singular) stiffness matrix of the RVE. $\hat{\mathbf{u}}^m$ is the non-reduced vector of generalised displacements containing both imposed and unknown DOFs of the FE model and $\hat{\mathbf{f}}^m$ is the non-reduced vector of generalised nodal forces (both known and unknown quantities). The expression of the above vectors and matrix is:

$$\begin{gathered} \hat{\mathbf{K}}^m := \begin{bmatrix} \mathbf{K}^m & \mathbf{K}^m_{\mathrm{BC}} \\ \mathbf{K}^{m\mathrm{T}}_{\mathrm{BC}} & \tilde{\mathbf{K}}^m \end{bmatrix},\ \hat{\mathbf{u}}^m := \begin{Bmatrix} \mathbf{u}^m \\ \mathbf{u}^m_{\mathrm{BC}} \end{Bmatrix},\ \hat{\mathbf{f}}^m := \begin{Bmatrix} \mathbf{f}^m \\ \mathbf{r}^m \end{Bmatrix}, \\ \mathbf{u}^m, \mathbf{f}^m \in \mathbb{R}^{N^m_{\mathrm{DOF}}},\ \mathbf{u}_{\mathrm{BC}^m}, \mathbf{r}^m \in \mathbb{R}^{N^m_{\mathrm{BC}}},\ \mathbf{K}^m \in \mathbb{R}^{N^m_{\mathrm{DOF}} \times N^m_{\mathrm{DOF}}}, \\ \mathbf{K}^m_{\mathrm{BC}} \in \mathbb{R}^{N^m_{\mathrm{DOF}} \times N^m_{\mathrm{BC}}},\ \tilde{\mathbf{K}}^m \in \mathbb{R}^{N^m_{\mathrm{BC}} \times N^m_{\mathrm{BC}}}. \end{gathered} \tag{11}$$

In Eq. (11), N^m_{DOF} is the number of unknown DOFs, while N^m_{BC} represents the number of DOFs where BCs on generalised displacements are applied (of course $\hat{N}^m_{\mathrm{DOF}} = N^m_{\mathrm{DOF}} + N^m_{\mathrm{BC}}$). $\mathbf{u}^m$ and $\mathbf{u}^m_{\mathrm{BC}}$ are the unknown and known vectors of generalised displacements, respectively. $\mathbf{f}^m$ is the vector of generalised external nodal forces, whilst $\mathbf{r}^m$ is the vector of generalised nodal reactions where BCs on generalised displacements are imposed. $\mathbf{K}^m$, $\mathbf{K}^m_{\mathrm{BC}}$ and $\tilde{\mathbf{K}}^m$ are the stiffness matrices of the FE model of the RVE after applying BCs. Inasmuch as the PBCs of Eq. (9) are imposed in terms of displacements and no external forces are applied to the FE model of the RVE, i.e. $\mathbf{f}^m = \mathbf{0}$, the equilibrium problem of Eq. (11) is of the Dirichlet's type.

The difference between the SEHM based on elements averaged stresses and the SEHM based on elements strain energy is in the post-processing of the results of the FE analyses. For both techniques, six static analyses, corresponding to the application of elementary uni-axial strain fields in Eq. (9), are required to uniquely assess the components of the macroscopic elasticity tensor $\mathbf{C}^M$ of the LS.
As far as the SEHM based on elements averaged stresses is concerned, for each static

analysis, the volume-averaged value of the stress vector (Voigt's notation) $\boldsymbol{\sigma}^m(\varepsilon^m_{\beta,0}) \in \mathbb{R}^6$ can be easily computed and the stiffness matrix of the equivalent homogeneous material can be calculated one column at time as:

$$\begin{aligned} &\mathbf{c}^M_\beta = \frac{1}{V_{\mathrm{RVE}}\varepsilon^m_{\beta,0}} \int_{V_{\mathrm{RVE}}} \boldsymbol{\sigma}^m(\varepsilon^m_{\beta,0})\, dV \approx \frac{1}{V_{\mathrm{RVE}}\varepsilon^m_{\beta,0}} \sum_{e=1}^{N^m_e} \boldsymbol{\sigma}^m_e(\varepsilon^m_{\beta,0}) V^m_e, \\ &\varepsilon^m_{\beta,0} \neq 0,\ \varepsilon^m_{\gamma,0} = 0,\ \beta,\gamma = 1,\cdots,6,\ \gamma \neq \beta,\ \mathbf{c}^M_\beta \in \mathbb{R}^6, \end{aligned} \tag{12}$$

where $\mathbf{c}^M_\beta$ represents the β column of matrix $\mathbf{C}^M$. In Eq. (12), N^m_e is the number of elements composing the FE model of the RVE, V^m_e is the volume of the generic element, whilst $V_{\mathrm{RVE}} = 8a^m_1 a^m_2 a^m_3$ is the "envelope" volume of the 3D domain wherein the RVE is defined.
Regarding the SEHM based on elements strain energy, the *compliance* (i.e. the work of internal forces) of the RVE can be easily retrieved for each static analysis as:

$$W^m := \mathbf{f}^{m\mathrm{T}}\mathbf{u}^m + \mathbf{r}^{m\mathrm{T}}\mathbf{u}^m_{\mathrm{BC}}. \tag{13}$$

Then, by considering both uni-axial and bi-axial strain fields in Eq. (9) and by imposing the equivalence between the strain energy of the equivalent homogeneous anisotropic continuum and that of the RVE of the LS, the components of matrix $\mathbf{C}^M$ can be computed as:

$$C^M_{kk} = \frac{W^m\left(\varepsilon^m_{k,0}\right)}{V_{\mathrm{RVE}}\left(\varepsilon^m_{k,0}\right)^2}, \quad k = 1,\ldots,6, \tag{14}$$

$$C^M_{ij} = \frac{W^m\left(\varepsilon^m_{i,0},\varepsilon^m_{j,0}\right)}{2V_{\mathrm{RVE}}\varepsilon^m_{i,0}\varepsilon^m_{j,0}} - C^M_{ii}\frac{\varepsilon^m_{i,0}}{2\varepsilon^m_{j,0}} - C^M_{jj}\frac{\varepsilon^m_{j,0}}{2\varepsilon^m_{i,0}}, \quad i,j = 1,\ldots,6. \tag{15}$$

Eq. (14) is used to assess the terms belonging to the main diagonal of tensor $\mathbf{C}^M$, whilst Eq. (15) allows for determining the terms outside the main diagonal. $W^m\left(\varepsilon^m_{k,0}\right)$ and $W^m\left(\varepsilon^m_{i,0},\varepsilon^m_{j,0}\right)$ represent the compliance, evaluated for uni-axial and bi-axial strain fields, respectively. Of course, Eq. (14) must be solved before Eq. (15); moreover the compliance of the RVE for a bi-axial strain field can be obtained from the results (displacements and forces) of the analyses wherein uni-axial strain fields are considered as follows:

$$W^m\left(\varepsilon^m_{i,0},\varepsilon^m_{j,0}\right) = \left(\mathbf{f}^{m\mathrm{T}}_i + \mathbf{f}^{m\mathrm{T}}_j\right)\left(\mathbf{u}^m_i + \mathbf{u}^m_j\right) + \left(\mathbf{r}^{m\mathrm{T}}_i + \mathbf{r}^{m\mathrm{T}}_j\right)\left(\mathbf{u}^m_{\mathrm{BC}i} + \mathbf{u}^m_{\mathrm{BC}j}\right), \tag{16}$$

where subscripts i and j refer to the FE analyses where uni-axial strain fields $\varepsilon^m_{i,0}$ and $\varepsilon^m_{j,0}$ are imposed in the PBCs of Eq. (9).
Finally, the density of the equivalent homogeneous anisotropic medium at the macroscopic is defined as:

$$\tau^M := \tau^m \frac{V^m}{V_{\mathrm{RVE}}}, \tag{17}$$

where τ^m is the density of the bulk material composing the RVE, whilst V^m is the actual volume of the RVE.

4. The multi-scale NURBS-based SIMP method

A detailed description of the mathematical background of the NURBS-based SIMP method is available in [47, 48]. The main features of the approach are briefly described here only for 3D multi-scale TO problems.
The goal of the multi-scale TO approach presented in this study is to determine the optimum topology of the LS RVE by considering design requirements involved at both lower (i.e. microscopic or mesoscopic) and upper (macroscopic) scales. The characteristic problem scales (and the relative geometrical features) are illustrated in Fig. 1.

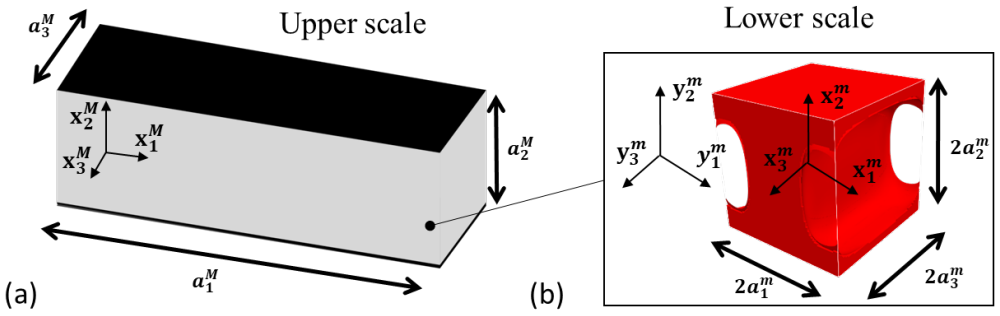

Figure 1: Characteristic scales of the multi-scale topology optimisation problem: (a) the macroscopic (upper) scale of the structure and (b) the lower (i.e. mesoscopic or microscopic) scale of the lattice RVE

Consider the compact Euclidean space $\mathcal{D}^m \subset \mathbb{R}^3$ (defining the RVE domain at the lower scale) in a Cartesian orthogonal frame $\mathrm{O}(y_1^m, y_2^m, y_3^m)$:

$$\mathcal{D}^m \coloneqq \{\mathbf{y}^{m\mathrm{T}} = (y_1^m, y_2^m, y_3^m) \in \mathbb{R}^3 : y_j^m \in [0, 2a_j^m],\ j = 1, 2, 3\}, \tag{18}$$

where a_j, is the characteristic length of the domain defined along x_j axis, as shown in Fig. 1. In the SIMP approach the *material domain* $\Omega^m \subseteq \mathcal{D}^m$ of the RVE is identified by means of the pseudo-density function $\rho(\mathbf{y}^m) \in [0, 1]$ for $\mathbf{y}^m \in \mathcal{D}^m$: $\rho(\mathbf{y}^m) = 0$ means absence of material, whilst $\rho(\mathbf{y}^m) = 1$ implies completely dense bulk material.

In the framework of the NURBS-based SIMP method, a NURBS entity of dimension $D + 1$ is used to describe the topology of a problem of dimension D. Therefore, if a 3D TO problem is considered, a 4D NURBS hyper-surface is needed to describe the RVE topology. In particular, the first three coordinates of the NURBS hyper-surface correspond to the Cartesian coordinates defining the 3D domain of the lattice RVE, while the fourth coordinate corresponds to the RVE pseudo-density field and reads:

$$\rho(\zeta_1^m, \zeta_2^m, \zeta_3^m) = \sum_{i_1=0}^{n_1} \sum_{i_2=0}^{n_2} \sum_{i_3=0}^{n_3} R_{i_1,i_2,i_3}(\zeta_1^m, \zeta_2^m, \zeta_3^m)\rho_{i_1,i_2,i_3}. \tag{19}$$

In Eq. (19), $n_{\mathrm{CP}} = (n_1 + 1)(n_2 + 1)(n_3 + 1)$ is the total number of CPs, while the dimensionless parameters ζ_j^m $(j = 1, 2, 3)$ can be related to the Cartesian coordinates y_j^m of the 3D domain (see Fig. 1) as follows:

$$\zeta_j^m = \frac{y_j^m}{2a_j^m},\ j = 1, 2, 3. \tag{20}$$

There are many parameters affecting the shape of a NURBS entity. Among them, the pseudo-density at CPs and the associated weights are identified as *design variables* and are collected in the vectors $\boldsymbol{\xi}_1$ and $\boldsymbol{\xi}_2$, respectively, defined as:

$$\boldsymbol{\xi}_1^{\mathrm{T}} \coloneqq (\rho_{0,0,0}, \cdots, \rho_{n_1,n_2,n_3}), \quad \boldsymbol{\xi}_2^{\mathrm{T}} \coloneqq (\omega_{0,0,0}, \cdots, \omega_{n_1,n_2,n_3}). \tag{21}$$

The cardinality of these arrays is $\sharp\boldsymbol{\xi}_1 = \sharp\boldsymbol{\xi}_2 = n_{\mathrm{CP}}$. Accordingly, in the most general case, the overall number of design variables is $n_{\mathrm{var}} = 2n_{\mathrm{CP}}$.

The multi-scale TO problem presented here deals with the minimisation of the macroscopic compliance W^M subject to an inequality constraint on the macroscopic mass m^M. Of course, the structure responses at the macroscopic scale are influenced by the topological variable defined at the lower scale as a result of the homogenisation process of the lattice RVE. As discussed in Section 3, the equilibrium of the RVE is described by Eq. (10) subject to the PBCs of Eq. (9), i.e. the RVE equilibrium problem is of Dirichlet's type. At the lower scale, the density field affects the element stiffness matrix and, accordingly, the global stiffness matrix of the FE model of the RVE as follows:

$$\hat{\mathbf{K}}^m = \sum_{e=1}^{N_e^m} \rho_e^{\alpha} \hat{\mathbf{L}}_e^{m\mathrm{T}} \mathbf{K}_e^m \hat{\mathbf{L}}_e^m, \quad \mathbf{K}_e^m \in \mathbb{R}^{N_{\mathrm{DOF},e}^m \times N_{\mathrm{DOF},e}^m}, \ \hat{\mathbf{L}}_e^m \in \mathbb{R}^{N_{\mathrm{DOF},e}^m \times \hat{N}_{\mathrm{DOF}}^m}, \tag{22}$$

where ρ_e is the fictitious density of Eq. (19) computed at the centroid of the generic element e and N_e^m is the total number of elements composing the FE model of the RVE. $\hat{\mathbf{L}}_e^m$ is the connectivity matrix of element e (before applying the BCs), $\mathbf{K}_e^m$ is the non-penalised element stiffness matrix expressed in the global reference frame of the model and $N_{\mathrm{DOF},e}^m$ is the number of DOFs for element e. In Eq. (22), $\alpha \geq 1$ is a suitable parameter that aims at penalising all the meaningless densities between 0 and 1, in agreement with the classic SIMP approach (usually $\alpha = 3$).
Conversely, the volume of the RVE is penalised as:

$$V^m = \sum_{e=1}^{N_e^m} \rho_e V_e^m, \tag{23}$$

where V_e^m is the volume of the generic element composing the RVE FE model.

At the macroscopic scale the equilibrium equation of the FE model of the structure reads:

$$\hat{\mathbf{K}}^M \hat{\mathbf{u}}^M = \hat{\mathbf{f}}^M; \quad \hat{\mathbf{u}}^M, \hat{\mathbf{f}}^M \in \mathbb{R}^{\hat{N}_{\mathrm{DOF}}^M}, \ \hat{\mathbf{K}}^M \in \mathbb{R}^{\hat{N}_{\mathrm{DOF}}^M \times \hat{N}_{\mathrm{DOF}}^M}, \tag{24}$$

where $\hat{N}_{\mathrm{DOF}}^M$ is the number of DOFs of the structure before the application of the BCs, while $\hat{\mathbf{K}}^M$ is the non-reduced stiffness matrix of the structure. $\hat{\mathbf{u}}^M$ is the non-reduced vector of generalised displacements containing both imposed and unknown DOFs of the FE model and $\hat{\mathbf{f}}^m$ is the non-reduced vector of generalised nodal forces (both known and

unknown quantities). In analogy with Eq. (11) the following arrays can be introduced:

$$\begin{gathered}\hat{\mathbf{K}}^M \coloneqq \begin{bmatrix} \mathbf{K}^M & \mathbf{K}^M_{\mathrm{BC}} \\ \mathbf{K}^{M\mathrm{T}}_{\mathrm{BC}} & \tilde{\mathbf{K}}^M \end{bmatrix}, \ \hat{\mathbf{u}}^M \coloneqq \begin{Bmatrix} \mathbf{u}^M \\ \mathbf{u}^M_{\mathrm{BC}} \end{Bmatrix}, \ \hat{\mathbf{f}}^M \coloneqq \begin{Bmatrix} \mathbf{f}^M \\ \mathbf{r}^M \end{Bmatrix}, \\ \mathbf{u}^M, \mathbf{f}^M \in \mathbb{R}^{N^M_{\mathrm{DOF}}}, \ \mathbf{u}_{\mathrm{BC}^M}, \mathbf{r}^M \in \mathbb{R}^{N^M_{\mathrm{BC}}}, \ \mathbf{K}^M \in \mathbb{R}^{N^M_{\mathrm{DOF}} \times N^M_{\mathrm{DOF}}}, \\ \mathbf{K}^M_{\mathrm{BC}} \in \mathbb{R}^{N^M_{\mathrm{DOF}} \times N^M_{\mathrm{BC}}}, \ \tilde{\mathbf{K}}^M \in \mathbb{R}^{N^M_{\mathrm{BC}} \times N^M_{\mathrm{BC}}},\end{gathered} \tag{25}$$

whose physical meaning is the same as the counterparts defined at the lower scale, see Section 3. Without loss of generality, in this work only non-null external nodal forces are applied at the macroscopic scale, whilst the imposed generalised displacements are null, i.e. $\mathbf{u}^M_{\mathrm{BC}} = \mathbf{0}$. Therefore, the equilibrium equation at the macroscopic scale simplifies to:

$$\mathbf{K}^M \mathbf{u}^M = \mathbf{f}^M. \tag{26}$$

As stated above, the pseudo-density field, defined at the RVE scale, affects also the macroscopic responses W^M and m^M through the macroscopic elasticity tensor $\mathbf{C}^M$ and the macroscopic density τ^M of the equivalent homogeneous anisotropic material, see Eq. (12) (or Eqs. (14) and (15)) and Eq. (17), respectively. Indeed, the reduced (i.e. non-singular) stiffness matrix $\mathbf{K}^M$ of the macroscopic FE model depends upon the tensor $\mathbf{C}^M$ as follows:

$$\mathbf{K}^M = \sum_{e=1}^{N^M_e} \mathbf{L}^{M\mathrm{T}}_e \int_{V^M_e} \mathbf{B}^{M\mathrm{T}}_e \mathbf{C}^M \mathbf{B}^M_e d\Omega \mathbf{L}^M_e, \ \ \mathbf{B}^M_e \in \mathbb{R}^{6 \times N^M_{\mathrm{DOF},e}}, \ \mathbf{L}^M_e \in \mathbb{R}^{N^M_{\mathrm{DOF},e} \times N^M_{\mathrm{DOF}}}. \tag{27}$$

In Eq. (27), N^M_e is the number of elements constituting the FE model at the macroscopic scale, whilst $N^M_{\mathrm{DOF},e}$ is the number of DOFs of the generic element. $\mathbf{L}^M_e$ is the connectivity matrix of element e, $\mathbf{B}^M_e$ is the matrix representing the product between the linear differential operator and the shape function matrices of the generic element and V^M_e is the volume of element e.
Moreover, the mass m^M of the macroscopic FE model reads:

$$m^M = \tau^M V^M = \tau^M \sum_{e=1}^{N^M_e} V^M_e. \tag{28}$$

where V^M is the overall volume of the FE model at the macroscopic scale. Therefore, the multi-scale TO problem focusing on the minimisation of the macroscopic compliance subject to an inequality constraint on the macroscopic mass can be formulated as a constrained

non-linear programming problem (CNLPP) as:

$$\min_{\boldsymbol{\xi}_1,\boldsymbol{\xi}_2} \frac{W^M}{W^M_{\text{ref}}}, \quad \text{s.t.}: \begin{cases} \mathbf{K}^M\mathbf{u}^M = \mathbf{f}^M, \quad \hat{\mathbf{K}}^m\hat{\mathbf{u}}^m = \hat{\mathbf{f}}^m, \\ g \coloneqq \dfrac{m^M}{m^M_{\text{ref}}} - \gamma \leq 0, \\ \xi_{1k} \in [\rho_{\min}, \rho_{\max}], \quad \xi_{2k} \in [\omega^m_{\min}, \omega^m_{\max}], \\ \forall k = 1, ..., n_{\text{CP}}. \end{cases} \tag{29}$$

In Eq. (29), m^M_{ref} and W^M_{ref} are reference values for the mass and the compliance of the structure at the macroscopic scale, respectively, whilst γ is the imposed mass fraction. $\rho_{\min}$ and $\rho_{\max}$ are the bounds on the density at each CP. In particular, the lower bound is imposed to the density field in order to prevent any singularity for the solution of the equilibrium problem at the lower scale. $\omega^m_{\min}$ and $\omega^m_{\max}$ are suitable lower and upper bounds on weights. Moreover, in Eq. (29), the linear index k has been introduced for the sake of compactness. The relationship between k and i_j, $(j = 1, 2, 3)$ is:

$$k \coloneqq 1 + i_1 + i_2(n_1 + 1) + i_3(n_1 + 1)(n_2 + 1). \tag{30}$$

The other NURBS parameters (i.e. degrees, knot-vector components and number of CPs) can be identified as *design parameters*, i.e. their value is set *a-priori* at the beginning of the TO and is not optimised: the interested reader is addressed to [48] for a deeper insight in the matter.

Remark 4.1. *As discussed in [51], one of the main advantages of the NURBS-based SIMP method is that the minimum length-scale manufacturing requirement can be easily integrated in the optimisation process* ***without adding an explicit constraint function*** *in the CNLPP formulation of Eq. (29). As explained in [51], the minimum length-scale constraint can be automatically satisfied by properly setting the integer parameters involved in the definition of the NURBS hyper-surface, i.e. the number of CPs and the degrees of the blending functions along each parametric direction, i.e. n_j and p_j, respectively. A meaningful example integrating this requirement is presented in Section 5.2.*

The computation of the derivatives of the objective function and the constraint function with respect to the design variables $\boldsymbol{\xi}_1$ and $\boldsymbol{\xi}_2$ is needed in order to solve problem (29) through a suitable deterministic algorithm. The gradient of g can be immediately inferred by considering Eqs. (17), (23) and (28):

$$\frac{\partial g}{\partial \xi_{ik}} = \tau^m \frac{V^M}{V_{\text{RVE}}} \sum_{e \in \mathcal{S}_k} V^m_j \frac{\partial \rho_e}{\partial \xi_{ik}}, \; i = 1, 2, \; k = 1, \cdots, n_{\text{CP}}, \tag{31}$$

where $\mathcal{S}_k$ is the discretised version of the local support of Eq. (8), while $\dfrac{\partial \rho_e}{\partial \xi_{ik}}$ reads

$$\frac{\partial \rho_e}{\partial \xi_{ik}} = \begin{cases} R^e_k, \text{ if } i = 1, \\ \dfrac{R^e_k}{\xi_{2k}} \left(\xi_{1k} - \rho_e\right), \text{ if } i = 2. \end{cases} \tag{32}$$

The scalar quantity R^e_k, appearing in Eq. (32), is the NURBS rational basis function of

Eq. (2) evaluated at the element centroid.

Conversely, the gradient of W^M requires a special attention. In order to derive its analytical expression, the NURBS local support property of Eq. (8) and the adjoint method [57] will be exploited. To this end, consider the following proposition.

Proposition 4.1. *Consider a deformable homogeneous anisotropic medium subject to* $\mathbf{f}^M \neq \mathbf{0}$ *and* $\mathbf{u}^M_{\text{BC}} = \mathbf{0}$*. If body forces are identically null, the gradient of the macroscopic compliance* W^M *with respect to the topological variable defined at the lower scale reads:*

$$\frac{\partial W^M}{\partial \xi_{ik}} = -\sum_{e=1}^{N_e^M}\sum_{q=1}^{6}\sum_{r=1}^{6}\frac{\partial C^M_{qr}}{\partial \xi_{ik}}\varepsilon^M_{eq}\varepsilon^M_{er}V_e^M, \qquad i=1,2,\ k=1,\cdots,n_{\text{CP}}, \tag{33}$$

with

$$\frac{\partial C^M_{qr}}{\partial \xi_{ik}} = \begin{cases} \dfrac{1}{V_{\text{RVE}}\left(\varepsilon^m_{q,0}\right)^2}\displaystyle\sum_{e\in\mathcal{S}_k}\frac{\alpha}{\rho_e}\frac{\partial \rho_e}{\partial \xi_{ik}}w_e^m\left(\varepsilon^m_{q,0}\right), \text{ if } q=r, \\ \dfrac{1}{2V_{\text{RVE}}\varepsilon^m_{q,0}\varepsilon^m_{r,0}}\displaystyle\sum_{e\in\mathcal{S}_k}\frac{\alpha}{\rho_e}\frac{\partial \rho_e}{\partial \xi_{ik}}w_e^m\left(\varepsilon^m_{q,0},\varepsilon^m_{r,0}\right) + \\ -\dfrac{\varepsilon^m_{q,0}}{2\varepsilon^m_{r,0}}\dfrac{\partial C^M_{qq}}{\partial \xi_{ik}} - \dfrac{\varepsilon^m_{r,0}}{2\varepsilon^m_{q,0}}\dfrac{\partial C^M_{rr}}{\partial \xi_{ik}}, \text{ if } q\neq r. \end{cases} \tag{34}$$

The proof of proposition 4.1 and the pseudo-code of the algorithm used to compute the gradient of W^M are provided in Appendix A.

Remark 4.2. *The quantity* ε^M_{eq} *appearing in Eq. (33) is the generic component of the macroscopic strain vector of element* e *defined as*

$$\boldsymbol{\varepsilon}^M_e \coloneqq \mathbf{B}^M_e\mathbf{L}^M_e\mathbf{u}^M, \tag{35}$$

while the quantity w^m_e *appearing in Eq. (34) is the compliance of the generic element of the FE model of the RVE at the lower scale.*

Remark 4.3. *As it can be inferred from Eq. (34), the SEHM based on elements strain energy has been used to assess the components of the macroscopic elasticity tensor of the LS. Indeed this technique reveals to be the most efficient choice (from a computational costs perspective) minimising the number of FE analyses required to assess matrix* $\mathbf{C}^M$ *as well as its gradient with respect to the topological variable at the RVE scale. In particular, as discussed in Appendix A, the* ***SEHM based on elements strain energy needs only seven static analyses per iteration*** *to compute the gradient of the macroscopic compliance: at the lower scale Eq. (10) must be solved six times (i.e. for each elementary strain field), while at the upper scale only one analysis is needed to solve Eq. (26). Conversely, as discussed in Appendix B,* ***the SEHM based on elements averaged stresses needs, at each iteration of the optimisation process, the resolution of 43 linear systems****: seven analyses at the lower scale, i.e. one for Eq. (10) and six for Eq. (B.21), which must be repeated six times (for each elementary strain field), plus one analysis at the macroscopic scale to solve Eq. (26).*

5. Numerical results

In this section, the effectiveness of the proposed method is tested on 2D and 3D benchmark problems. The results presented in this Section are obtained by means of the code SANTO (SIMP And NURBS for Topology Optimisation) developed at the I2M laboratory in Bordeaux [47, 48]. SANTO is coded in Python and it has been interfaced with ANSYS® software, which is used to build the FE models and assess the mechanical responses of the structure, at each pertinent scale. Moreover, the Method of Moving Asymptotes (MMA) algorithm [58] has been used to perform the solution search for CNLPP of Eq. (29). The parameters tuning the behaviour of the MMA algorithm as well as the user-defined convergence criteria are listed in Table 1.

Table 1: MMA algorithm parameters

Parameter	Value
move	0.2
albefa	0.1
asyntinit	0.5
asyincr	1.2
asydecr	0.7
Stop Criterion	**Value**
Maximum n. of function evaluations	$100 \times n_{\text{var}}$
Maximum n. of iterations	10000
Tolerance on objective function	1×10^{-6}
Tolerance on constraints	1×10^{-6}
Tolerance on input variables change	10^{-6}
Tolerance on Karush–Kuhn–Tucker norm	10^{-4}

Post-processing operations are performed in ParaView® environment. As far as numerical tests are concerned, the following aspects are considered:

1. The influence of the NURBS entity integer parameters, i.e. blending functions degree and CPs number, on the RVE optimised topology is investigated (only for 2D problems);
2. The influence of the geometric entity, i.e. B-spline or NURBS used to describe the pseudo-density field of the RVE, on the optimised topology is studied (both 2D and 3D problems);
3. The influence of the starting guess on the RVE optimised topology (only for 2D problems);
4. The influence of the macroscopic loads on the optimised topology of the RVE (both 2D and 3D problems).

Lower and upper bounds of design variables are set as: $\rho_{\min} = 10^{-3}$, $\rho_{\max} = 1$; $\omega_{\min} = 0.5$, $\omega_{\max} = 10$. Moreover, the non-trivial knot vectors components in Eq. (6) have been evenly distributed in the interval $[0, 1]$ for both 2D and 3D cases. For all benchmarks, the mass fraction at the macroscopic scale is $\gamma = 0.4$, while an aluminium alloy is used as a bulk material of the RVE with the following properties: $E^m = 71$ GPa, $\nu^m = 0.33$, $\tau^m = 2700$ Kgm^{-3}. The reference mass of the structure is defined as $m^M_{\text{ref}} = \tau^m V^m$, which corresponds to impose a unit pseudo-density field at the RVE scale in Eq. (23), while W^M_{ref} is the macroscopic compliance evaluated for the starting solution.

Furthermore, symmetry constraints on the pseudo-density field describing the RVE topology are imposed during optimisation: double symmetry for 2D problems (with respect to planes $y_j^m = \frac{a_j^m}{2}$, $j = 1, 2$) and three planes of symmetry ($y_j^m = \frac{a_j^m}{2}$, $j = 1, 2, 3$) for 3D problems in order to have an optimised topology characterised, at most, by an orthotropic behaviour. Of course, the presence of a symmetry constraints imply a reduction in the amount of design variables as follows:

$$n_{\text{var}} = \begin{cases} \prod_{i=1}^{N} \theta_i, \text{ for B} - \text{spline entity}, \\ 2 \prod_{i=1}^{N} \theta_i, \text{ for NURBS entity}, \end{cases} \tag{36}$$

with $N = 2$ and $N = 3$ for 2D and 3D problems, respectively and

$$\theta_i = \begin{cases} \dfrac{n_i + 1}{2}, \text{ if } n_i \text{ is even}, \\ \dfrac{n_i + 1}{2} + 1, \text{ otherwise}. \end{cases} \tag{37}$$

5.1. 2D benchmark problem

The geometry, loads and BCs of the 2D benchmark problem (indicated as 2D-BK in the following) considered in this study are illustrated in Fig. 2. It is a quarter of a square plate ($a_1^M = a_2^M = 100$ mm) with a hole of radius $R = \frac{a_1^M}{3}$. Uniform loads per unit length F_1^M and F_2^M are applied along sides AE and AB, respectively. The plate is subject to symmetric BCs on edges BC and DE. At the lower scale the RVE domain is a square of side $2a_1^m = 2a_2^m = 10$ mm. The RVE size has been chosen in order to have, at least, ten repetitive units along edges AB and AE.

The FE models at both upper and lower scales are made of PLANE182 elements (plane strain hypothesis, four nodes, two DOFs per node). The overall number of (quadrangular) elements composing the FE models at the macroscopic scale and at the RVE scale are $N_e^M = 1566$ and $N_e^m = 1600$, respectively.

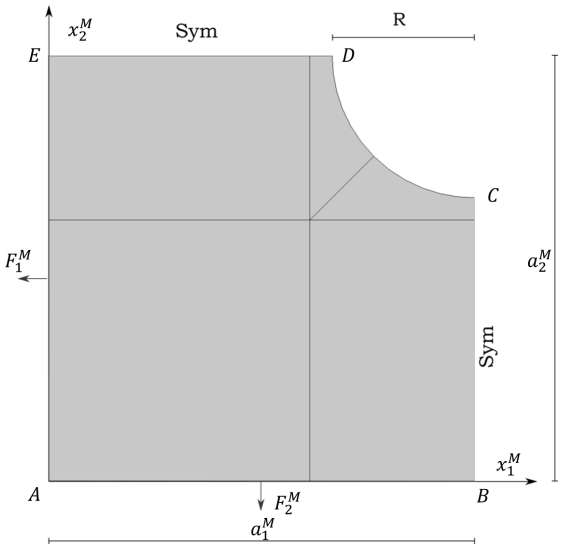

Figure 2: Geometry and boundary conditions of the benchmark problem 2D-BK

5.1.1. Sensitivity of the RVE topology to the NURBS entity integer parameters

Problem (29) is solved for 2D-BK by considering the following combinations of blending functions degrees and CPs numbers: (a) $p_j = 2, 3$, $(j = 1, 2)$; (b) $n_{\text{CP}} = 20 \times 20, 27 \times 27, 35 \times 35$. For this sensitivity analysis, the applied loads have been set as $F_1^M = 0$ and $F_2^M = 10$ Nmm^{-1}. An initial guess characterised by a uniform density field $\rho(\zeta_1^m, \zeta_2^m) = \gamma$ and $W_{\text{ref}}^M = 288.95$ Nmm has been considered for each analysis.
Results are provided in terms of macroscopic compliance W^M and number of iterations N_{iter} for B-spline and NURBS entities in Figs. 3 and 4, respectively. For each solution the requirement on the mass fraction is always satisfied and the solution is located on the boundary of the feasible domain.

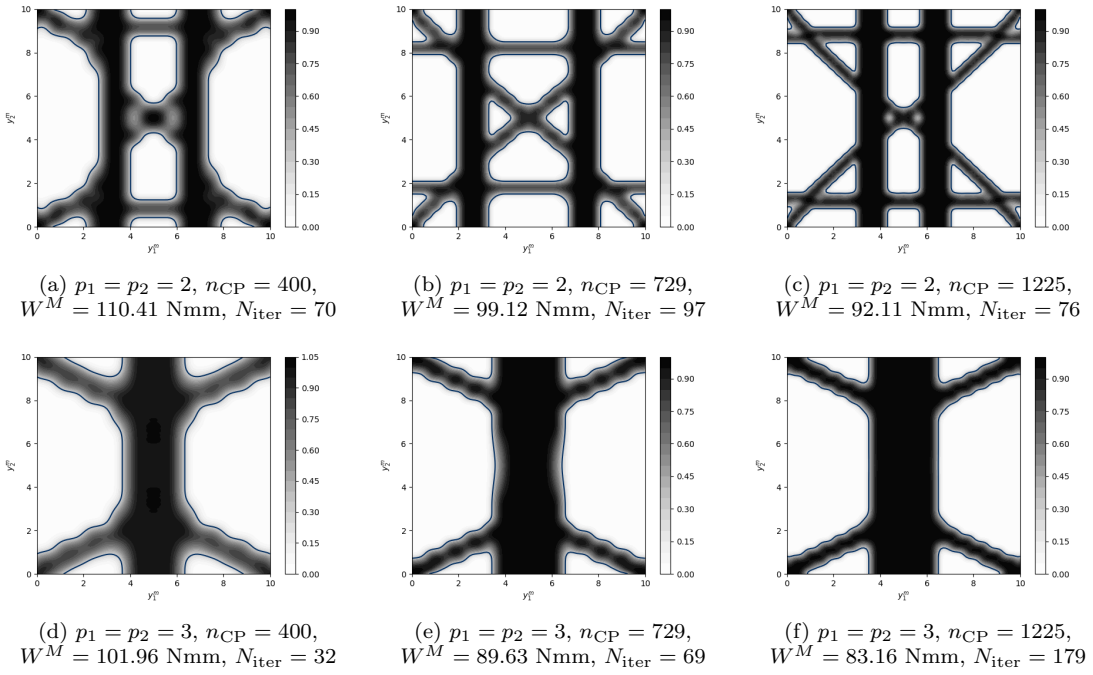

(a) $p_1 = p_2 = 2$, $n_{\text{CP}} = 400$, $W^M = 110.41$ Nmm, $N_{\text{iter}} = 70$

(b) $p_1 = p_2 = 2$, $n_{\text{CP}} = 729$, $W^M = 99.12$ Nmm, $N_{\text{iter}} = 97$

(c) $p_1 = p_2 = 2$, $n_{\text{CP}} = 1225$, $W^M = 92.11$ Nmm, $N_{\text{iter}} = 76$

(d) $p_1 = p_2 = 3$, $n_{\text{CP}} = 400$, $W^M = 101.96$ Nmm, $N_{\text{iter}} = 32$

(e) $p_1 = p_2 = 3$, $n_{\text{CP}} = 729$, $W^M = 89.63$ Nmm, $N_{\text{iter}} = 69$

(f) $p_1 = p_2 = 3$, $n_{\text{CP}} = 1225$, $W^M = 83.16$ Nmm, $N_{\text{iter}} = 179$

Figure 3: Benchmark problem 2D-BK: sensitivity of the optimised topology to CP numbers and basis functions degrees, B-spline solutions

A synthesis of the obtained results is illustrated in Fig. 5 in terms of the macroscopic compliance vs. CPs number and blending functions degrees.

The following remarks can be inferred from the results of the sensitivity analysis.

1. For B-spline solutions, the greater the number of control points the smaller the objective function value. However, unlike results presented in [47, 48] for the classical problem of the compliance minimisation subject to an inequality constraint of the volume fraction involving a single scale (i.e. the macroscopic one), the bigger the degree the smaller the objective function value.

2. Conversely, for NURBS solutions, a clear trend cannot be identified, unlike results presented in [47, 48]. In particular, as a general rule one can assert that the smaller the degree (or the higher the CPs number) the smaller the objective function value in agreement with the results for single-scale problems presented in [47, 48]. However, for some combinations of CPs number and degrees, the optimised solutions do not follow this general trend: this is probably due to the strong non-convexity of the

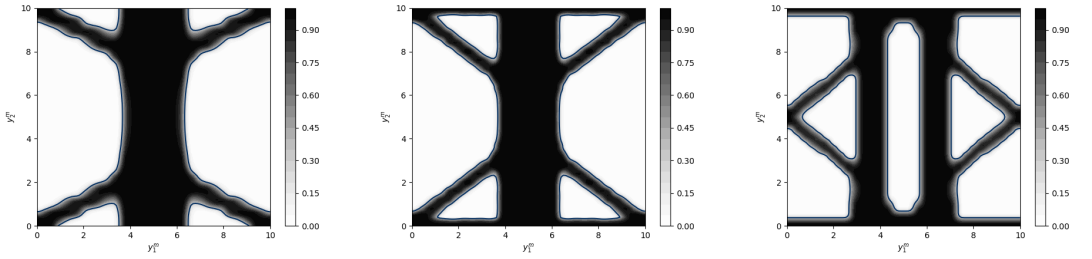

(a) $p_1 = p_2 = 2$, $n_{\text{CP}} = 400$, $W^M = 82.48$ Nmm, $N_{\text{iter}} = 43$

(b) $p_1 = p_2 = 2$, $n_{\text{CP}} = 729$, $W^M = 78.64$ Nmm, $N_{\text{iter}} = 95$

(c) $p_1 = p_2 = 2$, $n_{\text{CP}} = 1225$, $W^M = 88.37$ Nmm, $N_{\text{iter}} = 161$

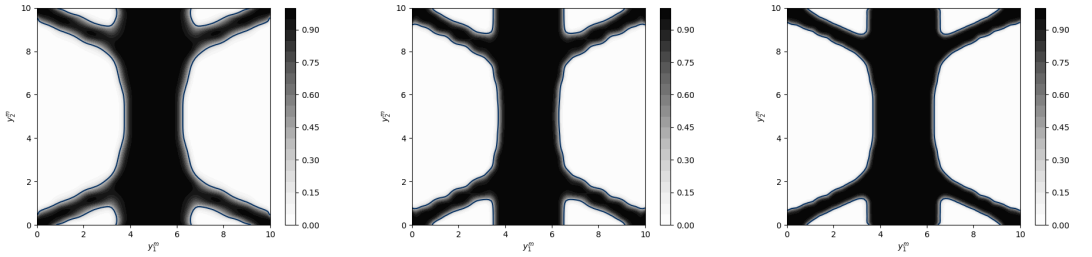

(d) $p_1 = p_2 = 3$, $n_{\text{CP}} = 400$, $W^M = 87.30$ Nmm, $N_{\text{iter}} = 100$

(e) $p_1 = p_2 = 3$, $n_{\text{CP}} = 729$, $W^M = 80.78$ Nmm, $N_{\text{iter}} = 90$

(f) $p_1 = p_2 = 3$, $n_{\text{CP}} = 1225$, $W^M = 76.90$ Nmm, $N_{\text{iter}} = 250$

Figure 4: Benchmark problem 2D-BK: sensitivity of the optimised topology to CP numbers and basis functions degrees, NURBS solutions

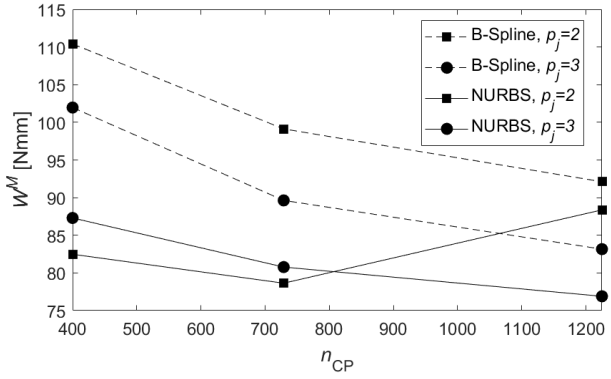

Figure 5: Benchmark problem 2D-BK: compliance vs. CPs number and degrees for B-spline and NURBS solutions

multi-scale TO problem of Eq. (29), which show several local feasible minimiser as discussed in the next subsection.

3. The CPs number and basis functions degree along each direction affect the size of the local support, see Eq. (8), which enforces a minimum member size requirement in the optimised topology, as discussed in [51]. As far as this point is concerned, the same remarks as in [51] can be made: the higher the degree (or the smaller the CPs number) the greater the local support, thus each CP affects a wider region of the mesh during optimisation. Moreover, the higher the degree the smoother the topology boundary after CAD reconstruction. Conversely, small degrees (or a high CP number) produce optimised topologies characterised by thin branches. Therefore, as a general rule, a high number of CPs and small degrees should be considered if

minimum member size does not constitute a restriction for the problem at hand. High degrees and/or small CPs number should be considered otherwise.

4. Optimised topologies obtained using NURBS surfaces are characterised by values of the objective function lower or equal than those resulting from B-spline surfaces when considering the same number of CPs and the same degrees, as shown in Fig. 5. In particular, from the analysis of Figs. 3 and 4, it appears that NURBS topologies have a boundary smoother than that of B-spline solutions, for each case.
5. Fig. 6 illustrates the outstanding advantages provided by the NURBS-based SIMP method. On the one hand the topology is unrelated from the mesh of the FE model and it is represented by a purely geometrical entity, i.e. a 3D NURBS surface. On the other hand, the NURBS surface is a CAD-compatible entity which can be easily exported into any CAD software to rebuild in a straightforward way the boundary of the optimised 2D structure. This task can be achieved by evaluating a threshold value for the density function meeting the optimisation constraint (this operation is automatically done by the SANTO algorithm at the end of the optimisation process).

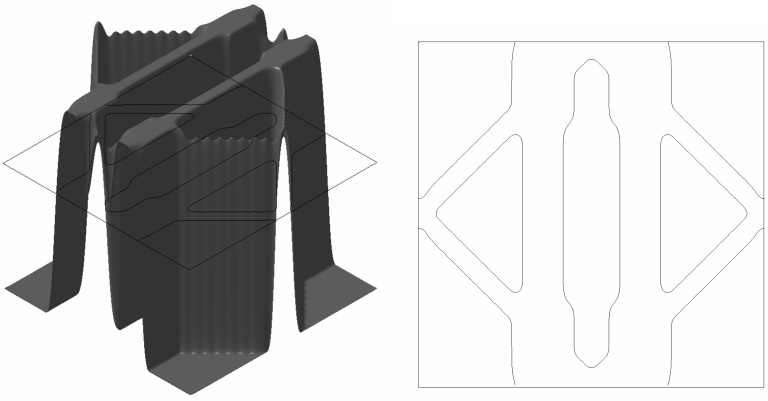

(a) NURBS surface and cutting plane (b) The 2D optimised topology

Figure 6: Benchmark problem 2D-BK: CAD model of the RVE optimised topology for a NURBS surface with $p_1 = p_2 = 2$ and $n_{\text{CP}} = 1225$

5.1.2. Sensitivity of the RVE topology to the initial guess

Unlike the standard CNLPP dealing with the compliance minimisation subject to a constraint on the volume fraction involving a single-scale analysis [47, 48], the CNLPP of Eq. (29) shows a highly non-convex behaviour. To (numerically) prove its non-convexity, the influence of the starting point on the optimised topology is discussed here. The analysis is carried out for both B-spline and NURBS solutions characterised by the following parameters: $p_1 = p_2 = 2$, $n_{\text{CP}} = 35 \times 35$. The applied loads are set as $F_1^M = 0$ and $F_2^M = 10$ Nmm^{-1}.

For each B-spline/NURBS solution, two feasible starting points have been considered. The first one consists of a topology having one hole (where the pseudo-density is equal to $\rho_{\min}$) satisfying the constraint on the mass ratio and characterised by $W_{\text{ref}}^M = 271.47$ Nmm. The second starting point is characterised by two holes and by a reference macroscopic compliance $W_{\text{ref}}^M = 271.16$ Nmm.

Results are provided in terms of macroscopic compliance W^M and number of iterations N_{iter} for B-spline and NURBS entities in Fig. 7. For each solution the requirement on the

mass fraction is always satisfied and the solution is located on the boundary of the feasible domain.

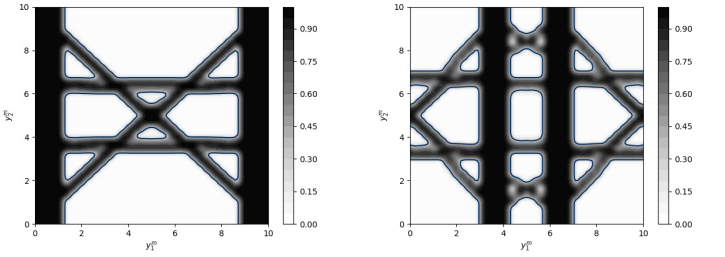

(a) one hole, $W^M = 87.35$ Nmm, $N_{\text{iter}} = 45$

(b) two holes, $W^M = 96.32$ Nmm, $N_{\text{iter}} = 170$

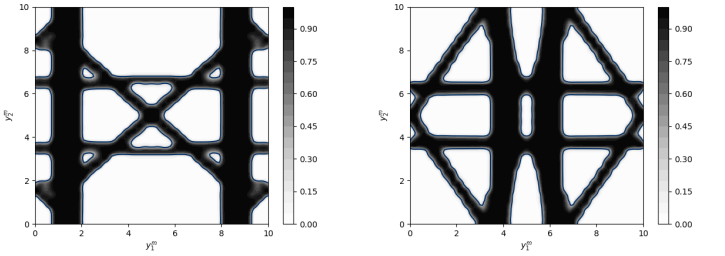

(c) one hole, $W^M = 79.79$ Nmm, $N_{\text{iter}} = 147$

(d) two holes, $W^M = 82.87$ Nmm, $N_{\text{iter}} = 110$

Figure 7: Benchmark problem 2D-BK: influence of the initial guess on the optimised topology for (a)-(b) B-spline and (c)-(d) NURBS solutions with $p_1 = p_2 = 2$ and $n_{\text{CP}} = 1225$

As it can been inferred from Fig. 7, the choice of the initial guess has a strong impact on the optimised topology. On the one hand, for the same number of CPs and the same degrees and under the considered loads and BCs, choosing an initial guess with one hole allows finding results better (in terms of W^M) than those characterising the optimised solutions shown in Figs. 3c and 4c (obtained by starting from a uniform pseudo-density field). On the other hand, for the same values of the NURBS entity integer parameters, the choice of a different starting point has a strong impact on the convergence rate of the MMA algorithm, which converges towards the nearest local (feasible) minimiser.

5.1.3. Sensitivity of the RVE topology to the macroscopic loading condition

Problem (29) is solved for 2D-BK by considering different combinations of the applied loads: (a) $\frac{F_1^M}{F_2^M} = 0$ and $F_2^M = 10$ Nmm^{-1} (presented in the above subsections); (b) $\frac{F_1^M}{F_2^M} = 0.5$ and $F_2^M = 10$ Nmm^{-1}; (c) $\frac{F_1^M}{F_2^M} = 1$ and $F_2^M = 10$ Nmm^{-1}; (d) $\frac{F_1^M}{F_2^M} \to \infty$ and $F_1^M = 10$ Nmm^{-1}. The goal of these analyses is to highlight the effect of the macroscopic loading condition on the optimised topology of the RVE at the lower scale.

Problem (29) has been solved using both B-spline and NURBS entities having degrees $p_1 = p_2 = 3$ and an overall number of CPs $n_{\text{CP}} = 35 \times 35$. An initial guess characterised by a uniform density field $\rho(\zeta_1^m, \zeta_2^m) = \gamma$ and $W_{\text{ref}}^M = 288.95$ Nmm has been considered for each analysis.

The numerical results regarding the case $\frac{F_1^M}{F_2^M} = 0$ are illustrated in Figs. 3f and 4f. As far as the other cases are concerned, results are provided in terms of macroscopic compliance W^M for B-spline and NURBS entities in Fig. 8. For each solution the requirement on the

mass fraction is always satisfied and the solution is located on the boundary of the feasible domain.

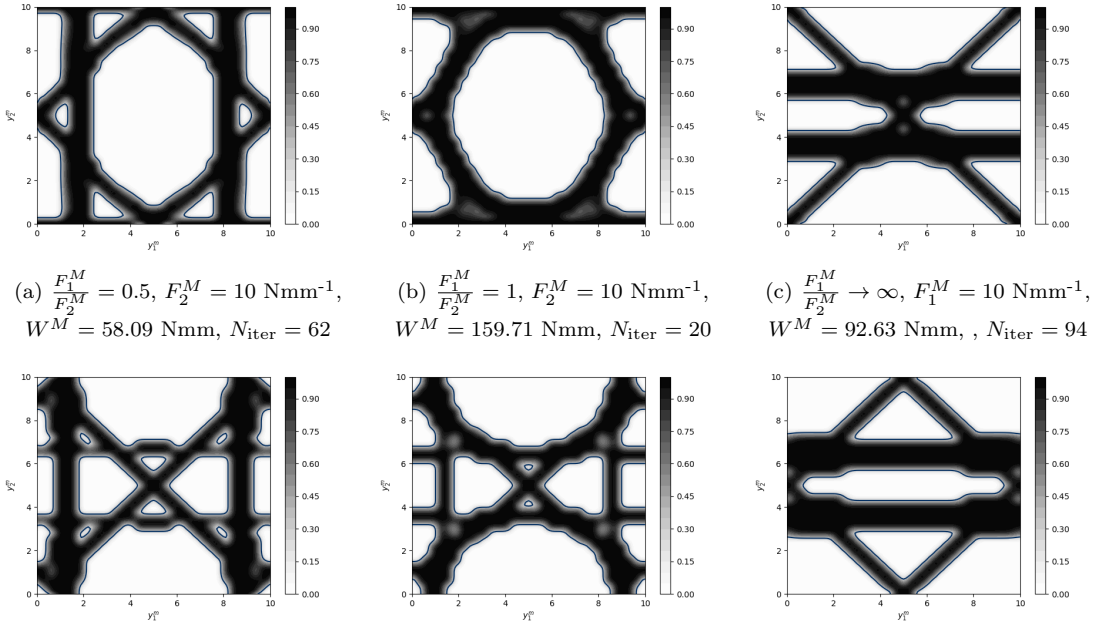

(a) $\frac{F_1^M}{F_2^M} = 0.5$, $F_2^M = 10$ Nmm^{-1}, $W^M = 58.09$ Nmm, $N_{\text{iter}} = 62$

(b) $\frac{F_1^M}{F_2^M} = 1$, $F_2^M = 10$ Nmm^{-1}, $W^M = 159.71$ Nmm, $N_{\text{iter}} = 20$

(c) $\frac{F_1^M}{F_2^M} \to \infty$, $F_1^M = 10$ Nmm^{-1}, $W^M = 92.63$ Nmm, , $N_{\text{iter}} = 94$

(d) $\frac{F_1^M}{F_2^M} = 0.5$, $F_2^M = 10$ Nmm^{-1}, $W^M = 42.30$ Nmm, $N_{\text{iter}} = 46$

(e) $\frac{F_1^M}{F_2^M} = 1$, $F_2^M = 10$ Nmm^{-1}, $W^M = 145.37$ Nmm, $N_{\text{iter}} = 153$

(f) $\frac{F_1^M}{F_2^M} \to \infty$, $F_1^M = 10$ Nmm^{-1}, $W^M = 78.20$ Nmm, $N_{\text{iter}} = 116$

Figure 8: Benchmark problem 2D-BK: influence of the macroscopic loading condition on the RVE optimised topology for (a)-(c) B-spline and (d)-(e) NURBS solutions with $p_1 = p_2 = 3$ and $n_{\text{CP}} = 1225$

As it can been inferred from Fig. 8, the macroscopic loading condition has a strong influence on the RVE optimised topology at the lower scale. In particular, in order to properly withstand the applied loads at the macroscopic scale and to minimise W^M, the RVE topology evolves in such a way to optimise the macroscopic elastic response of the continuum. In particular, for each considered loading condition, the matrix $\mathbf{C}^M$ related to the optimised topology is characterised by the most efficient elastic symmetry with respect to the applied loads. Indeed, the elastic constants for each topology are reported in Table 2. As expected, the optimised topologies of the RVE for cases $\frac{F_1^M}{F_2^M} = 0$ and $\frac{F_1^M}{F_2^M} \to \infty$ show

Table 2: 2D-BK: elastic constants for the optimised topologies in the case $p_1 = p_2 = 3$, $n_{\text{CP}} = 1225$ for each loading condition

Elastic constant	$\frac{F_1^M}{F_2^M} = 0$		$\frac{F_1^M}{F_2^M} = 0.5$		$\frac{F_1^M}{F_2^M} = 1$		$\frac{F_1^M}{F_2^M} \to \infty$	
	B-spline	NURBS	B-spline	NURBS	B-spline	NURBS	B-spline	NURBS
E_1^M [MPa]	6258.90	6487.57	5976.94	6163.72	10214.03	8352.45	17514.38	19468.20
E_2^M [MPa]	18246.18	16515.65	15610.41	15544.38	10273.89	8643.90	2808.68	2781.78
G_{12}^M [MPa]	1348.89	1411.84	2410.54	2776.16	2365.72	2299.19	2713.64	2599.40
ν_{12}^M	0.29	0.27	0.44	0.48	0.41	0.44	0.14	0.12

a macroscopic orthotropic behaviour with the main orthotropy axis oriented along axis x_2^M and x_1^M, respectively. The macroscopic elasticity tensor of the optimised topologies of the RVE for the case $\frac{F_1^M}{F_2^M} = 1$ is characterised by a square symmetry, i.e. $E_1^M \approx E_2^M$ (but the

RVE has not a macroscopic isotropic behaviour because $G_{12}^M \neq \frac{E_1^M}{2(1+\nu_{12}^M)}$) for both B-spline and NURBS solutions (although the optimised topologies are really different). Finally, the RVE topologies for the case $\frac{F_1^M}{F_2^M} = 0.5$ are characterised by a macroscopic orthotropic behaviour with a higher value of the Young's modulus along the x_2^M axis. Finally, for each loading condition, NURBS solutions are characterised by a value of the merit function lower than that of the B-spline counterpart.

5.2. 3D benchmark problem

The geometry, loads and BCs of the 3D benchmark problem (indicated as 3D-BK in the following) considered in this study are illustrated in Fig. 9. As shown in this figure, the optimisation domain at the macroscopic scale is a cube of side $a_i^M = 300$ mm ($i = 1, 2, 3$), which is meshed with SOLID185 elements (eight nodes, three DOFs per node, reduced integration): the element size is 10 mm for an overall number of $N_e^M = 27000$ elements. Moreover, the cube is clamped at the nodes A, B, C and D corresponding to the vertices of the bottom face.
As illustrated in Fig. 9, problem (29) is solved for 3D-BK by considering two load cases (LCs): in the first one (LC1) only traction loads P along x_2^M axis are applied on nodes E, F, G, H and I belonging to the top face, whilst in the second one (LC2) shear forces P are applied on nodes E, F, G, H (in order to generate a non-zero torque) and a traction load P is still applied on node I. The idea is to investigate the influence of the macroscopic loading condition on the optimised RVE topology at the lower scale. The value of the force applied on the generic node is $P = 300$ N.

At the lower scale the RVE domain is a cube of side $2a_1^m = 2a_2^m = 2a_3^m = 10$ mm. The RVE size has been chosen in order to have, at least, 30 repetitive units along the generic axis x_i^M at the macroscopic scale. The RVE model has been meshed with $N_e^m = 8000$ SOLID185 elements.

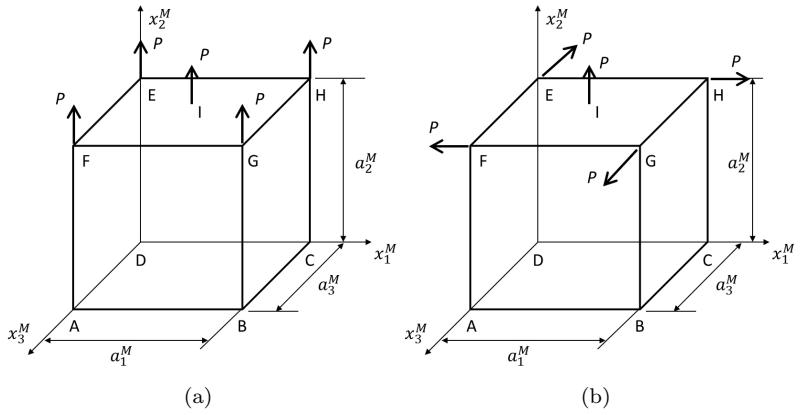

Figure 9: Geometry and boundary conditions of the benchmark problem 3D-BK: (a) only axial forces are applied at the macroscopic scale, (b) axial and shear forces are applied at the macroscopic scale

For both LCs, the CNLPP of Eq. (29) has been enhanced by considering a constraint on the minimum length scale requirement: the minimum dimension of the optimised topology should be greater than or equal to $d_{\min}^m = 0.5$ mm. To automatically satisfy the minimum length scale requirement without introducing an explicit constraint in the problem formulation, according to the methodology presented in [51], B-spline and NURBS entities with $p_j = 3$ ($j = 1, 2, 3$) and $n_{\text{CP}} = 18 \times 18 \times 18$ are used for these analyses. Moreover, an

initial guess characterised by a uniform density field $\rho(\zeta_1^m, \zeta_2^m, \zeta_3^m) = \gamma$ has been selected. The reference macroscopic compliance is $W^M_{\text{ref}} = 692.29$ Nmm for the first load case and $W^M_{\text{ref}} = 504.94$ for the second one.
Numerical results are provided in terms of macroscopic compliance W^M, number of iterations N_{iter} and measured minimum member size, i.e. $d^m_{\text{min-meas}}$, for B-spline and NURBS entities in Fig. 10 (the topology illustrated in Fig. 10d has been cut with the plane $y_1^m = \frac{a_1^m}{2}$ in order to show the internal structure of the RVE). For each solution the requirement on the mass fraction is always satisfied and the solution is located on the boundary of the feasible domain.

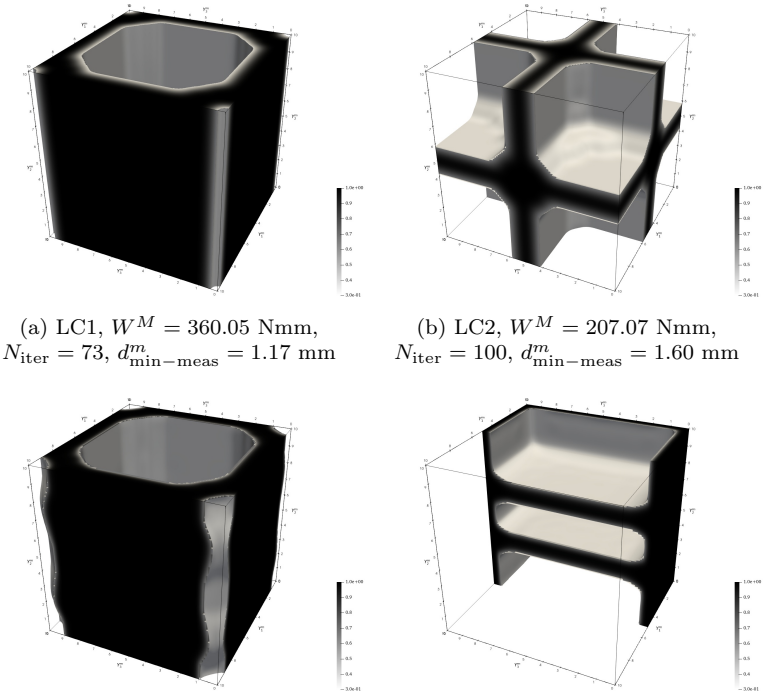

(a) LC1, $W^M = 360.05$ Nmm, $N_{\text{iter}} = 73$, $d^m_{\text{min-meas}} = 1.17$ mm

(b) LC2, $W^M = 207.07$ Nmm, $N_{\text{iter}} = 100$, $d^m_{\text{min-meas}} = 1.60$ mm

(c) LC1, $W^M = 301.05$ Nmm, $N_{\text{iter}} = 77$, $d^m_{\text{min-meas}} = 1.0$ mm

(d) LC2, $W^M = 164.58$ Nmm, $N_{\text{iter}} = 100$, $d^m_{\text{min-meas}} = 0.5$ mm

Figure 10: Benchmark problem 3D-BK: influence of the loading condition at the macroscopic scale on the RVE optimised topology for (a)-(b) B-spline and (c)-(d) NURBS solutions with $p_1 = p_2 = p_3 = 3$ and $n_{\text{CP}} = 5832$

As it can been inferred from Fig. 10, the macroscopic loading condition has a strong influence on the RVE optimised topology at the lower scale.
Firstly, it must be pointed out that NURBS solutions show better performances than the B-spline counterparts, regardless of the considered LC. Moreover, thanks to the geometrical properties of the NURBS blending functions, the requirement on the minimum length scale is always satisfied. In particular, it is noteworthy that the minimum length scale constraint is active for the NURBS solution illustrated in Fig. 10d.
Secondly, in order to properly withstand the applied loads at the macroscopic scale and to minimise W^M, the RVE topology evolves in such a way to optimise the macroscopic elastic response of the continuum. As a consequence, for each LC, the matrix $\mathbf{C}^M$ related to the optimised topology is characterised by the most efficient elastic symmetry for that case. The elastic constants for each topology are reported in Table 3.

As expected, the optimised RVE topologies (B-spline and NURBS solutions) for LC1

Table 3: 3D-BK: elastic constants for the optimised topologies in the case $p_1 = p_2 = p_3 = 3$ and $n_{\text{CP}} = 5832$ for each load case

Elastic constant	LC1		LC2	
	B-spline	NURBS	B-spline	NURBS
E_1^M [MPa]	12375.13	13575.96	15648.95	19134.29
E_2^M [MPa]	21792.07	25179.94	14704.77	14268.34
E_3^M [MPa]	12375.23	13599.33	15648.95	19134.34
G_{12}^M [MPa]	4895.14	5829.61	3161.04	3083.47
G_{13}^M [MPa]	610.23	773.16	3466.19	5176.82
G_{23}^M [MPa]	4895.17	5840.89	3161.04	3083.43
ν_{12}^M	0.19	0.18	0.19	0.20
ν_{13}^M	0.11	0.19	0.20	0.24
ν_{23}^M	0.33	0.33	0.18	0.15

show a macroscopic orthotropic behaviour with the main orthotropy axis aligned with the load direction, i.e. x_2^M axis. The Young's moduli E_1^M and E_3^M, the shear moduli G_{12}^M and G_{23}^M as well as the Poisson's coefficients ν_{12}^M and $\nu_{32}^M = \nu_{23}^M \frac{E_3^M}{E_2^M}$ are equal but the material does not show a transverse isotropic behaviour because $G_{13}^M \neq \frac{E_1^M}{2\left(\nu_{13}^M+1\right)}$. The macroscopic elasticity tensor of B-spline and NURBS solutions for LC2 are still orthotropic, but with a value of the Young's moduli E_1^M and E_3^M higher than E_2^M (which implies that the main orthotropy direction is no longer aligned with the x_2^M axis) and with a higher value of the shear modulus G_{13}^M in order to withstand shear loads (and the resulting torque).

6. Conclusion

In this work, multi-scale TO problems of LSs have been formulated in an innovative SIMP algorithm based on NURBS entities. In particular, the proposed approach consider the topological variable defined only at the lattice RVE scale, while physical responses can be defined at each pertinent scale of the LS, depending on the requirements of the problem at hand. The proposed approach is based on NURBS hyper-surfaces, on the standard FE method and on the SEHM involving elements strain energy to perform the scale transition.

Some features of the proposed framework need to be highlighted.

- Three main advantages of the NURBS formalism can be clearly identified: (a) unlike the classical SIMP approach, there is no need to define a further filter zone, as the NURBS local support establishes an implicit relationship among contiguous mesh elements, (b) when compared to the classical SIMP approach, the number of design variables is reduced and (c) the CAD reconstruction phase is straightforward.

- A sensitivity analysis of the optimised topology of the RVE to the NURBS integer parameters has been performed. Unlike the classical problem of the compliance minimisation subject to a constraint on the volume fraction stated on a single scale, when B-spline entities are employed to describe the pseudo-density field of the RVE, the greater the number of CPs (for a given degree) or the bigger the degree (for a given number of CPs) the smaller the objective function value. Conversely, when NURBS entities are used to describe the RVE topological variable, no general rules

can be defined and the results seem to approximately satisfy the global trend observed in previous works (i.e. the smaller the degree or the higher the CPs number the lower the objective function value). Moreover, an excellent trade-off between computational costs and performances of the final solution can be achieved by using a CPs number equal to three-quarters of the number of mesh elements.

- The role of NURBS weights has been assessed. In particular, by considering same number of CPs and degrees, the objective function of the NURBS solution is lower than the B-spline counterpart, and the boundary of the NURBS solution is smoother than that of the B-spline solution.
- The influence of the initial guess has been taken into account. Particularly, multi-scale TO problems are strongly non-convex and are characterised by several local minima. Therefore, a particular care must be put in the choice of the (feasible) initial guess and multiple optimisation calculations (by using different starting points) should be performed in order to find an efficient local minimiser.
- The macroscopic loading condition strongly influences the optimised topology of the RVE. In particular, in order to satisfy the requirements of the problem at hand and to withstand the applied loads, the RVE topology evolves towards a configuration optimising the macroscopic elastic response of the continuum.
- The minimum-length scale requirement is correctly taken into account, without introducing an explicit optimisation constraint, by properly setting the integer parameters of the NURBS entity.
- The better performances, in terms of computational costs when used in the framework of multi-scale TO, of the SEHM based on elements strain energy over the SEHM based on elements averaged stresses have been rigorously proven.

As far as prospects are concerned, this paper is far from being exhaustive on the topic of multi-scale analyses and LS design by means of TO. Firstly, the proposed methodology should be extended to the case of multi-scale TO problems where topological variables are defined at different scales. To this end, in the framework of the NURBS-based SIMP method, the number of NURBS entities should be equal, at least, to the number of scales, involved into the problem formulation, wherein the definition of a topological variable makes sense. The relationships occurring among these entities (i.e. the topological variables defined at different scales) should be carefully determined in order to correctly state the optimisation problem and to satisfy the hypotheses at the basis of the SEHM.
Secondly, pertinent manufacturing requirements, related to the additive manufacturing process, should be integrated into the multi-scale TO problem formulation, especially in terms of the RVE geometrical features, e.g. overhang angle, admissible curvature, etc.
Finally, suitable failure criteria should be formulated for the homogeneous anisotropic material at the macroscopic scale and integrated in the multi-scale TO problem formulation. Furthermore, in order to identify the most critical regions at the macroscopic scale and to transfer the local stress/strain field to the lattice RVE a modified SEHM with a strong coupling between scales should be developed and integrated in the optimisation process.

Acknowledgements

G. Bertolino is grateful to French National Research Agency, which has funded part of the activities presented in this paper through the project COFFA ANR-17-CE10-0008. T. Roiné is grateful to Nouvelle-Aquitaine through the OCEAN-ALM project.

Data availability

The raw/processed data required to reproduce these findings cannot be shared at this time as the data also forms part of an ongoing study.

A. Compliance gradient for multi-scale problems

The proof of Proposition 4.1 is given here below.

Proof. Inasmuch as body forces are identically null, the derivative of the right-hand side of Eq. (26) is

$$\frac{\partial \mathbf{f}^M}{\partial \xi_{ik}} = \mathbf{0},\ i = 1, 2,\ k = 1, ..., n_{\mathrm{CP}}, \tag{A.1}$$

which implies the following equality

$$\frac{\partial \left(\mathbf{K}^M \mathbf{u}^M\right)}{\partial \xi_{ik}} = \mathbf{0} \ \Rightarrow \frac{\partial \mathbf{u}^M}{\partial \xi_{ik}} = -(\mathbf{K}^M)^{-1} \frac{\partial \mathbf{K}^M}{\partial \xi_{ik}} \mathbf{u}^M. \tag{A.2}$$

The macroscopic compliance is defined as:

$$W^M \coloneqq \mathbf{f}^{M\mathrm{T}} \mathbf{u}^M. \tag{A.3}$$

By taking into account for Eqs. (A.1) and (A.2), the derivative of W^M reads

$$\frac{\partial W^M}{\partial \xi_{ik}} = \mathbf{f}^{M\mathrm{T}} \frac{\partial \mathbf{u}^M}{\partial \xi_{ik}} = -\mathbf{u}^{M\mathrm{T}} \frac{\partial \mathbf{K}^M}{\partial \xi_{ik}} \mathbf{u}^M. \tag{A.4}$$

By injecting the expression of $\mathbf{K}^M$ of Eq. (27) in the above formula and by considering the expression of $\boldsymbol{\varepsilon}_e^M$ of Eq. (35) one gets:

$$\begin{aligned} \frac{\partial W^M}{\partial \xi_{ik}} &= -\sum_{e=1}^{N_e^M} \int_{V_e^M} \boldsymbol{\varepsilon}_e^{M\mathrm{T}} \frac{\partial \mathbf{C}^M}{\partial \xi_{ik}} \boldsymbol{\varepsilon}_e^M d\Omega \\ &\approx -\sum_{e=1}^{N_e^M} \sum_{q=1}^{6} \sum_{r=1}^{6} \frac{\partial C_{qr}^M}{\partial \xi_{ik}} \varepsilon_{eq}^M \varepsilon_{er}^M V_e^M. \end{aligned} \tag{A.5}$$

Inasmuch as the SEHM based on elements strain energy is used in this work, the derivatives of the components C_{qr}^M of the macroscopic elasticity tensor can be easily calculated from Eqs. (14) and (15):

$$\frac{\partial C_{qr}^M}{\partial \xi_{ik}} = \begin{cases} \dfrac{1}{V_{\mathrm{RVE}} \left(\varepsilon_{q,0}^m\right)^2} \dfrac{\partial W^m \left(\varepsilon_{q,0}^m\right)}{\partial \xi_{ik}},\ \text{if } q = r, \\ \dfrac{1}{2V_{\mathrm{RVE}} \varepsilon_{q,0}^m \varepsilon_{r,0}^m} \dfrac{\partial W^m \left(\varepsilon_{q,0}^m, \varepsilon_{r,0}^m\right)}{\partial \xi_{ik}} + \\ -\dfrac{\varepsilon_{q,0}^m}{2\varepsilon_{r,0}^m} \dfrac{\partial C_{qq}^M}{\partial \xi_{ik}} - \dfrac{\varepsilon_{r,0}^m}{2\varepsilon_{q,0}^m} \dfrac{\partial C_{rr}^M}{\partial \xi_{ik}},\ \text{if } q \neq r. \end{cases} \tag{A.6}$$

The next passage consists of expressing the derivative of the compliance at the lower scale, i.e. $\frac{\partial W^m}{\partial \xi_{ik}}$. Since Eqs. (10) and (11) hold, the compliance of the RVE can be expressed as:

$$\begin{aligned} W^m =& \mathbf{f}^{m\mathrm{T}}\mathbf{u}^m + \mathbf{u}_{\mathrm{BC}}^{m\mathrm{T}}\mathbf{r}^m + \boldsymbol{\eta}^{\mathrm{T}}\left(\mathbf{K}^m\mathbf{u}^m + \mathbf{K}_{\mathrm{BC}}^m\mathbf{u}_{\mathrm{BC}}^m - \mathbf{f}^m\right) + \\ &+ \boldsymbol{\lambda}^{\mathrm{T}}\left(\mathbf{K}_{\mathrm{BC}}^{m\mathrm{T}}\mathbf{u}^m + \tilde{\mathbf{K}}^m\mathbf{u}_{\mathrm{BC}}^m - \mathbf{r}^m\right), \end{aligned} \tag{A.7}$$

where $\boldsymbol{\eta}^m \in \mathbb{R}^{N_{\mathrm{DOF}}^m}$ and $\boldsymbol{\lambda}^m \in \mathbb{R}^{N_{\mathrm{BC}}^m}$ are two arbitrary vectors. Under the hypothesis that vectors $\mathbf{f}^m$ and $\mathbf{u}_{\mathrm{BC}}^m$ do not depend on the topological variable, i.e.

$$\frac{\partial \mathbf{f}^m}{\partial \xi_{ik}} = \mathbf{0}, \quad \frac{\partial \mathbf{u}_{\mathrm{BC}}^m}{\partial \xi_{ik}} = \mathbf{0}, \tag{A.8}$$

the derivative of Eq. (A.7) reads:

$$\begin{aligned} \frac{\partial W^m}{\partial \xi_{ik}} =& \mathbf{f}^{m\mathrm{T}}\frac{\partial \mathbf{u}^m}{\partial \xi_{ik}} + \mathbf{u}_{\mathrm{BC}}^{m\mathrm{T}}\frac{\partial \mathbf{r}^m}{\partial \xi_{ik}} + \\ &+ \boldsymbol{\eta}^{\mathrm{T}}\left(\frac{\partial \mathbf{K}^m}{\partial \xi_{ik}}\mathbf{u}^m + \mathbf{K}^m\frac{\partial \mathbf{u}^m}{\partial \xi_{ik}} + \frac{\partial \mathbf{K}_{\mathrm{BC}}^m}{\partial \xi_{ik}}\mathbf{u}_{\mathrm{BC}}^m\right) + \\ &+ \boldsymbol{\lambda}^{\mathrm{T}}\left(\frac{\partial \mathbf{K}_{\mathrm{BC}}^{m\mathrm{T}}}{\partial \xi_{ik}}\mathbf{u}^m + \mathbf{K}_{\mathrm{BC}}^{m\mathrm{T}}\frac{\partial \mathbf{u}^m}{\partial \xi_{ik}} + \frac{\partial \tilde{\mathbf{K}}^m}{\partial \xi_{ik}}\mathbf{u}_{\mathrm{BC}}^m - \frac{\partial \mathbf{r}^m}{\partial \xi_{ik}}\right). \end{aligned} \tag{A.9}$$

In Eq. (A.9), vectors $\boldsymbol{\eta}$ and $\boldsymbol{\lambda}$ can be chosen such that the terms multiplying $\frac{\partial \mathbf{u}^m}{\partial \xi_{ik}}$ and $\frac{\partial \mathbf{r}^m}{\partial \xi_{ik}}$ vanish, i.e.

$$\begin{aligned} &\boldsymbol{\lambda} = \mathbf{u}_{\mathrm{BC}}^m, \\ &\mathbf{K}^m\boldsymbol{\eta} = -\mathbf{f}^m - \mathbf{K}_{\mathrm{BC}}^m\boldsymbol{\lambda} = -\mathbf{f}^m - \mathbf{K}_{\mathrm{BC}}^m\mathbf{u}_{\mathrm{BC}}^m = \mathbf{K}^m\mathbf{u}^m - 2\mathbf{f}^m. \end{aligned} \tag{A.10}$$

By injecting Eq. (A.10) in Eq. (A.9) one obtains:

$$\begin{aligned} \frac{\partial W^m}{\partial \xi_{ik}} =& \mathbf{u}^{m\mathrm{T}}\frac{\partial \mathbf{K}^m}{\partial \xi_{ik}}\mathbf{u}^m + 2\mathbf{u}^{m\mathrm{T}}\frac{\partial \mathbf{K}_{\mathrm{BC}}^m}{\partial \xi_{ik}}\mathbf{u}_{\mathrm{BC}}^m + \mathbf{u}_{\mathrm{BC}}^{m\mathrm{T}}\frac{\partial \tilde{\mathbf{K}}^m}{\partial \xi_{ik}}\mathbf{u}_{\mathrm{BC}}^m + \\ &- 2\mathbf{f}^{m\mathrm{T}}(\mathbf{K}^m)^{-1}\left(\frac{\partial \mathbf{K}^m}{\partial \xi_{ik}}\mathbf{u}^m + \frac{\partial \mathbf{K}_{\mathrm{BC}}^m}{\partial \xi_{ik}}\mathbf{u}_{\mathrm{BC}}^m\right). \end{aligned} \tag{A.11}$$

Inasmuch as the PBCs of Eq. (9) are imposed in terms of displacements and no external forces are applied to the FE model of the RVE, i.e. $\mathbf{f}^m = \mathbf{0}$, and since Eqs. (10) and (11) hold, Eq. (A.11) simplifies to:

$$\frac{\partial W^m}{\partial \xi_{ik}} = \hat{\mathbf{u}}^{m\mathrm{T}}\frac{\partial \hat{\mathbf{K}}^m}{\partial \xi_{ik}}\hat{\mathbf{u}}^m. \tag{A.12}$$

By considering the expression of the non-reduced stiffness matrix of the FE model of the RVE of Eq. (22) and by taking advantage from the local support property of Eq. (8), the

above formula becomes:

$$\begin{aligned}\frac{\partial W^m}{\partial \xi_{ik}} &= \sum_{e\in\mathcal{S}_k} \frac{\alpha}{\rho_e}\frac{\partial \rho_e}{\partial \xi_{ik}} \rho_e^{\alpha} \hat{\mathbf{u}}^{m\mathrm{T}} \hat{\mathbf{L}}_e^{m\mathrm{T}} \mathbf{K}_e^m \hat{\mathbf{L}}_e^m \hat{\mathbf{u}}^m \\ &= \sum_{e\in\mathcal{S}_k} \frac{\alpha}{\rho_e}\frac{\partial \rho_e}{\partial \xi_{ik}} \hat{\mathbf{u}}_e^{m\mathrm{T}} \hat{\mathbf{f}}_e^m = \sum_{e\in\mathcal{S}_k} \frac{\alpha}{\rho_e}\frac{\partial \rho_e}{\partial \xi_{ik}} w_e^m,\end{aligned} \tag{A.13}$$

where $\hat{\mathbf{u}}_e^m$, $\hat{\mathbf{f}}_e^m \in \mathbb{R}^{N_{\mathrm{DOF},e}^m}$ are the generalised nodal displacements and forces of element e, while w_e^m is the compliance of element e. Finally, by injecting Eq. (A.13), evaluated for each elementary strain field, into Eq. (A.6), one can easily retrieve Eq. (34) and this last passage concludes the proof. ■

It is noteworthy that, when the SEHM based on elements strain energy is used, the assessment of the gradient of the macroscopic compliance requires the resolution of seven static analyses, i.e. six static analyses to get the macroscopic elasticity tensor $\mathbf{C}^M$, by solving Eq. (10) for each elementary strain field $\varepsilon_{r,0}^m$, $(r = 1, \cdots, 6)$, and one static analysis at the macroscopic scale by solving Eq. (26). Therefore, for each iteration of the optimisation process, Algorithm 1 is invoked to carry out all the necessary steps for computing the gradient of W^M.

Algorithm 1 Computation of the gradient of W^M.

Set $\varepsilon_{r,0}^m = 0$, $\forall r = 1, \cdots, 6$
for $r = 1, \cdots, 6$ **do**
    Set $\varepsilon_{r,0}^m \neq 0$
    Solve Eq. (10) and get $\hat{\mathbf{u}}_e^m\left(\varepsilon_{r,0}^m\right)$, $\hat{\mathbf{f}}_e^m\left(\varepsilon_{r,0}^m\right)$, $w_e^m\left(\varepsilon_{r,0}^m\right)$, $\forall e = 1, \cdots, N_e^m$
    Calculate C_{rr}^M from Eq. (14)
    Calculate $\dfrac{\partial C_{rr}^M}{\partial \xi_{ik}}$ from the first of Eq. (34)
end for
for $q = 1, \cdots, 6$ **do**
    for $r = q, \cdots, 6$, **do**
        Calculate $W^m\left(\varepsilon_{q,0}^m, \varepsilon_{r,0}^m\right)$ from Eq. (16)
        Calculate C_{qr}^M from Eq. (15), set $C_{rq}^M = C_{qr}^M$
        Calculate $w_e^m\left(\varepsilon_{q,0}^m, \varepsilon_{r,0}^m\right) = \left[\hat{\mathbf{u}}_e^{m\mathrm{T}}\left(\varepsilon_{q,0}^m\right) + \hat{\mathbf{u}}_e^{m\mathrm{T}}\left(\varepsilon_{r,0}^m\right)\right]\left[\hat{\mathbf{f}}_e^m\left(\varepsilon_{q,0}^m\right) + \hat{\mathbf{f}}_e^m\left(\varepsilon_{r,0}^m\right)\right]$, $\forall e$
        Calculate $\dfrac{\partial C_{qr}^M}{\partial \xi_{ik}}$ from the second of Eq. (34)
    end for
end for
Solve Eq. (26) and get ε_e^M, $\forall e = 1, \cdots, N_e^M$
Calculate $\dfrac{\partial W^M}{\partial \xi_{ik}}$ from Eq. (33)

B. On the computational costs of the strain energy homogenisation method

As stated in Appendix A, the SEHM based on elements strain energy needs only seven static analyses per iteration to compute the gradient of the macroscopic compliance $\dfrac{\partial W^M}{\partial \xi_{ik}}$.

Conversely, the SEHM based on elements averaged stresses needs a higher computational effort. In order to understand this point, consider the r-th column of the macroscopic elasticity tensor of Eq. (12). It can be rewritten as

$$\begin{aligned}\mathbf{c}_r^M =& \frac{1}{V_{\mathrm{RVE}}\varepsilon_{r,0}^m}\sum_{e=1}^{N_e^m}\boldsymbol{\sigma}_e^m(\varepsilon_{r,0}^m)V_e^m + \\ &+ \boldsymbol{\mu}^T\left(\mathbf{K}^m\mathbf{u}^m(\varepsilon_{r,0}^m) + \mathbf{K}_{\mathrm{BC}}^m\mathbf{u}_{\mathrm{BC}}^m(\varepsilon_{r,0}^m)\right),\end{aligned} \tag{B.14}$$

because the second term of the right-hand side of the above formula is identically zero (recall that the equilibrium problem of the RVE is of the Dirichlet's type, i.e. $\mathbf{f}^m = \mathbf{0}$). In Eq. (B.14), $\boldsymbol{\mu} \in \mathbb{R}^{N_{\mathrm{DOF}}^m \times 6}$ is the arbitrary adjoint matrix. The derivative of Eq. (B.14) is:

$$\begin{aligned}\frac{\partial \mathbf{c}_r^M}{\partial \xi_{ik}} =& \frac{1}{V_{\mathrm{RVE}}\varepsilon_{r,0}^m}\sum_{e=1}^{N_e^m}\frac{\partial\boldsymbol{\sigma}_e^m}{\partial\xi_{ik}}V_e^m + \\ &+ \boldsymbol{\mu}^T\left(\frac{\partial\mathbf{K}^m}{\partial\xi_{ik}}\mathbf{u}^m + \mathbf{K}^m\frac{\partial\mathbf{u}^m}{\partial\xi_{ik}} + \frac{\partial\mathbf{K}_{\mathrm{BC}}^m}{\partial\xi_{ik}}\mathbf{u}_{\mathrm{BC}}^m\right).\end{aligned} \tag{B.15}$$

The derivative of $\boldsymbol{\sigma}_e^m$ can be assessed by considering its expression:

$$\boldsymbol{\sigma}_e^m \coloneqq \rho_e^\alpha\mathbf{C}^m\mathbf{B}_e^m\hat{\mathbf{L}}_e^m\hat{\mathbf{u}}^m, \tag{B.16}$$

where $\mathbf{C}^m$ is the elasticity matrix of the bulk material composing the RVE. The derivative of Eq. (B.16) reads:

$$\frac{\partial\boldsymbol{\sigma}_e^m}{\partial\xi_{ik}} = \frac{\alpha}{\rho_e}\frac{\partial\rho_e}{\partial\xi_{ik}}\boldsymbol{\sigma}_e^m + \rho_e^\alpha\mathbf{C}^m\mathbf{B}_e^m\hat{\mathbf{L}}_e^m\frac{\partial\hat{\mathbf{u}}^m}{\partial\xi_{ik}}, \tag{B.17}$$

which, due to Eq. (A.8), can be simplified to:

$$\frac{\partial\boldsymbol{\sigma}_e^m}{\partial\xi_{ik}} = \frac{\alpha}{\rho_e}\frac{\partial\rho_e}{\partial\xi_{ik}}\boldsymbol{\sigma}_e^m + \rho_e^\alpha\mathbf{C}^m\mathbf{B}_e^m\mathbf{L}_e^m\frac{\partial\mathbf{u}^m}{\partial\xi_{ik}}, \tag{B.18}$$

where $\mathbf{L}_e^m \in \mathbb{R}^{N_{\mathrm{DOF},e}^m \times N_{\mathrm{DOF}}^m}$ is the connectivity matrix obtained by suppressing N_{BC} columns, corresponding to the imposed displacements, from matrix $\hat{\mathbf{L}}_e^m$. By injecting Eq. (B.18) in Eq. (B.15) and by taking into account for the local support property of Eq. (8) one obtains:

$$\begin{aligned}\frac{\partial \mathbf{c}_r^M}{\partial \xi_{ik}} =& \frac{1}{V_{\mathrm{RVE}}\varepsilon_{r,0}^m}\sum_{e\in\mathcal{S}_k}\frac{\partial\rho_e}{\partial\xi_{ik}}\boldsymbol{\sigma}_e^m V_e^m + \boldsymbol{\iota}\frac{\partial\mathbf{u}^m}{\partial\xi_{ik}} + \\ &+ \boldsymbol{\mu}^T\left(\frac{\partial\mathbf{K}^m}{\partial\xi_{ik}}\mathbf{u}^m + \mathbf{K}^m\frac{\partial\mathbf{u}^m}{\partial\xi_{ik}} + \frac{\partial\mathbf{K}_{\mathrm{BC}}^m}{\partial\xi_{ik}}\mathbf{u}_{\mathrm{BC}}^m\right),\end{aligned} \tag{B.19}$$

where $\boldsymbol{\iota}$ is defined as

$$\boldsymbol{\iota} \coloneqq \frac{1}{V_{\mathrm{RVE}}\varepsilon_{r,0}^m}\sum_{e=1}^{N_e^m}V_e^m\rho_e^\alpha\mathbf{C}^m\mathbf{B}_e^m\mathbf{L}_e^m,\ \boldsymbol{\iota} \in \mathbb{R}^{6\times N_{\mathrm{DOF}}^m}. \tag{B.20}$$

In Eq. (B.19), the matrix $\boldsymbol{\mu}$ can be chosen such that the term multiplying $\dfrac{\partial \mathbf{u}^m}{\partial \xi_{ik}}$ vanishes, i.e.

$$\mathbf{K}^m \boldsymbol{\mu} = -\boldsymbol{\iota}^{\mathrm{T}}, \tag{B.21}$$

which corresponds to six linear systems where the unknowns are the column vectors composing the matrix $\boldsymbol{\mu}$, i.e $\boldsymbol{\mu} = \{\boldsymbol{\mu}_1, \cdots, \boldsymbol{\mu}_6\}$, with $\boldsymbol{\mu}_i \in \mathbb{R}^{N^m_{\mathrm{DOF}}}$. Finally, by injecting Eq. (B.21) into Eq. (B.19), one obtains:

$$\frac{\partial \mathbf{c}^M_r}{\partial \xi_{ik}} = \frac{1}{V_{\mathrm{RVE}} \varepsilon^m_{r,0}} \sum_{e \in \mathcal{S}_k} \frac{\partial \rho_e}{\partial \xi_{ik}} \boldsymbol{\sigma}^m_e V^m_e + \boldsymbol{\mu}^T \left(\frac{\partial \mathbf{K}^m}{\partial \xi_{ik}} \mathbf{u}^m + \frac{\partial \mathbf{K}^m_{\mathrm{BC}}}{\partial \xi_{ik}} \mathbf{u}^m_{\mathrm{BC}} \right). \tag{B.22}$$

It is noteworthy that the computation of the macroscopic compliance derivative $\dfrac{\partial W^M}{\partial \xi_{ik}}$ when using the SEHM based on elements averaged stresses requires, at each iteration of the optimisation process, the resolution of 43 linear systems: seven analyses, consisting of Eqs. (10) and (B.21), for each one of the six elementary strain fields plus the macroscopic FE analysis to solve Eq. (26).

References

[1] M. Askari, D. A. Hutchins, P. J. Thomas, L. Astolfi, R. L. Watson, M. Abdi, M. Ricci, S. Laureti, L. Nie, S. Freear, R. Wildman, C. Tuck, M. Clarke, E. Woods, A. T. Clare, Additive manufacturing of metamaterials: A review, Additive Manufacturing (2020) 101562.
URL https://doi.org/10.1016/j.addma.2020.101562

[2] W. Wu, W. Hu, G. Qian, H. Liao, X. Xu, F. Berto, Mechanical design and multifunctional applications of chiral mechanical metamaterials: A review, Materials & Design 180 (2019) 107950.
URL https://doi.org/10.1016/j.matdes.2019.107950

[3] L. Dong, Mechanical responses of Ti-6Al-4V cuboctahedral truss lattice structures, Composite Structures 235 (2020).
URL https://doi.org/10.1016/j.compstruct.2019.111815

[4] L. Azzouz, Y. Chen, M. Zarrelli, J. M. Pearce, L. Mitchell, G. Ren, M. Grasso, Mechanical properties of 3-d printed truss-like lattice biopolymer non-stochastic structures for sandwich panels with natural fibre composite skins, Composite Structures 213 (2019) 220 – 230.

[5] Y. Liu, Z. Dong, J. Ge, X. Lin, J. Liang, Stiffness design of a multilayer arbitrary bcc lattice structure with face sheets, Composite Structures 230 (2019).
URL https://doi.org/10.1016/j.compstruct.2019.111485

[6] C. Peng, P. Tran, H. Nguyen-Xuan, A. Ferreira, Mechanical performance and fatigue life prediction of lattice structures: Parametric computational approach, Composite Structures 235 (2020).
URL https://doi.org/10.1016/j.compstruct.2019.111821

[7] J. Tkac, S. Samborski, K. Monkova, H. Debski, Analysis of mechanical properties of a lattice structure produced with the additive technology, Composite Structures 242

(2020).
URL https://doi.org/10.1016/j.compstruct.2020.112138

[8] G. Bertolino, M. Montemurro, G. D. Pasquale, Multi-scale shape optimisation of lattice structures: an evolutionary-based approach, International Journal on Interactive Design and Manufacturing 13 (4) (2019) 1565–1578.

[9] K. Refai, M. Montemurro, C. Brugger, N. Saintier, Determination of the effective elastic properties of titanium lattice structures, Mechanics of Advanced Materials and Structures (2019).
URL https://doi.org/10.1080/15376494.2018.1536816

[10] M. Bendsoe, N. Kikuchi, Generating optimal topologies in structural design using a homogenization method, Computer Methods in Applied Mechanics and Engineering 71 (1988) 197–224.

[11] K. Suzuki, N. Kikuchi, A homogenization method for shape and topology optimization, Computer Methods in Applied Mechanics and Engineering 93 (3) (1991) 291 – 318.

[12] G. Allaire, E. Bonnetier, G. Francfort, F. Jouve, Shape optimization by the homogenization method, Numerische Mathematik 76 (1997) 27–68.

[13] Y. Xie, G. Steven, A simple evolutionary procedure for structural optimization, Computers & Structures 49 (5) (1993) 885 – 896.

[14] X. Yang, Y. Xie, G. Steven, O. Querin, Bidirectional evolutionary method for stiffness optimization, AIAA Journal 37 (1999) 1483–1488.

[15] Y. M. Huang, X.and Xie, Evolutionary topology optimization of continuum structures with an additional displacement constraint, Structural and Multidisciplinary Optimization 40 (2009).
URL https://doi.org/10.1007/s00158-009-0382-4

[16] X. Huang, M. Xie, Evolutionary topology optimization of continuum structures: Methods and applications, John Wiley & Sons (2010) 121–150.

[17] D. Da, L. Xia, G. Li, X. Huang, Evolutionary topology optimization of continuum structures with smooth boundary representation, Structural and Multidisciplinary Optimization 57 (6) (2018) 2143–2159.

[18] M. de Ruiter, F. van Keulen, Topology optimization using a topology description function, Structural and Multidisciplinary Optimization 26 (6) (2004) 406–416.

[19] G. Allaire, F. Jouve, A.-M. Toader, Structural optimization using sensitivity analysis and a level-set method, Journal of Computational Physics 194 (1) (2004) 363 – 393.

[20] N. P. van Dijk, K. Maute, M. Langelaar, F. van Keulen, Level-set methods for structural topology optimization: a review, Structural and Multidisciplinary Optimization 48 (3) (2013) 437–472.

[21] M. Bendsoe, O. Sigmund, Topology Optimization - Theory, Methods and Applications, Springer, 2003.

[22] O. Sigmund, A 99 line topology optimization code written in Matlab, Structural and Multidisciplinary Optimization 21 (2) (2001) 120–127.

[23] G. Allaire, P. Geoffroy-Donders, O. Pantz, Topology optimization of modulated and oriented periodic microstructures by the homogenization method, Computers & Mathematics with Applications 78 (7) (2019) 2197 – 2229.

[24] P. Geoffroy-Donders, G. Allaire, O. Pantz, 3-d topology optimization of modulated and oriented periodic microstructures by the homogenization method, Journal of Computational Physics 401 (2020).
URL https://doi.org/10.1016/j.jcp.2019.108994

[25] C. Nguyen, X. Zhuang, L. Chamoin, X. Zhao, H. Nguyen-Xuan, T. Rabczuk, Three-dimensional topology optimization of auxetic metamaterial using isogeometric analysis and model order reduction, Computer Methods in Applied Mechanics and Engineering 371 (2020).
URL https://doi.org/10.1016/j.cma.2020.113306

[26] Y. Zhang, M. Xiao, X. Zhang, L. Gao, Topological design of sandwich structures with graded cellular cores by multiscale optimization, Computer Methods in Applied Mechanics and Engineering 361 (2020).
URL https://doi.org/10.1016/j.cma.2019.112749

[27] J. Gao, H. Li, L. Gao, M. Xiao, Topological shape optimization of 3d micro-structured materials using energy-based homogenization method, Advances in Engineering Software 116 (2018) 89–102.

[28] J. Liu, Y. Zheng, R. Ahmad, J. Tang, Y. Ma, Minimum length scale constraints in multi-scale topology optimisation for additive manufacturing, Virtual and Physical Prototyping 14 (3) (2019) 229–241.

[29] R. Picelli, R. Sivapuram, S. Townsend, H. A. Kim, Stress Topology Optimisation for Architected Material Using the Level Set Method, in: Advances in Structural and Multidisciplinary Optimization, Springer International Publishing, 2017, pp. 1254–1269.

[30] P. Vogiatzis, S. Chen, X. Wang, T. Li, L. Wang, Topology optimization of multi-material negative poisson's ratio metamaterials using a reconciled level set method, Computer-Aided Design 83 (2017) 15 – 32.

[31] J. K. Guest, J. H. Prévost, Optimizing multifunctional materials: Design of microstructures for maximized stiffness and fluid permeability, International Journal of Solids and Structures 43 (22-23) (2006) 7028–7047.

[32] R. Yang, J. Du, Microstructural topology optimization with respect to sound power radiation, Structural and Multidisciplinary Optimization 47 (2) (2012) 191–206.

[33] Y. Zhang, M. Xiao, H. Li, L. Gao, Topology optimization of material microstructures using energy-based homogenization method under specified initial material layout, Journal of Mechanical Science and Technology 33 (2) (2019) 677–693.

[34] M. Collet, L. Noël, M. Bruggi, P. Duysinx, Topology optimization for microstructural design under stress constraints, Structural and Multidisciplinary Optimization 58 (6) (2018) 2677–2695.

[35] L. Xia, P. Breitkopf, Design of materials using topology optimization and energy-based homogenization approach in matlab, Structural and Multidisciplinary Optimization 52 (6) (2015) 1229–1241.

[36] X. Huang, A. Radman, Y. Xie, Topological design of microstructures of cellular materials for maximum bulk or shear modulus, Computational Materials Science 50 (6) (2011) 1861–1870.

[37] J. Xu, L. Gao, M. Xiao, J. Gao, H. Li, Isogeometric topology optimization for rational design of ultra-lightweight architected materials, International Journal of Mechanical Sciences 166 (2020).
URL https://doi.org/10.1016/j.ijmecsci.2019.105103

[38] Y. Du, H. Li, Z. Luo, Q. Tian, Topological design optimization of lattice structures to maximize shear stiffness, Advances in Engineering Software 112 (2017) 211–221.

[39] J. Gao, M. Xiao, L. Gao, J. Yan, W. Yan, Isogeometric topology optimization for computational design of re-entrant and chiral auxetic composites, Computer Methods in Applied Mechanics and Engineering 362 (2020) 112876.

[40] Y. Zheng, Y. Wang, X. Lu, Z. Liao, J. Qu, Evolutionary topology optimization for mechanical metamaterials with auxetic property, International Journal of Mechanical Sciences 179 (2020).
URL https://doi.org/10.1016/j.ijmecsci.2020.105638

[41] H. Yu, J. Huang, B. Zou, W. Shao, J. Liu, Stress-constrained shell-lattice infill structural optimisation for additive manufacturing, Virtual and Physical Prototyping 15 (1) (2019) 35–48.

[42] R. Sivapuram, P. D. Dunning, H. A. Kim, Simultaneous material and structural optimization by multiscale topology optimization, Structural and Multidisciplinary Optimization 54 (5) (2016) 1267–1281.

[43] Y. Wang, H. Xu, D. Pasini, Multiscale isogeometric topology optimization for lattice materials, Computer Methods in Applied Mechanics and Engineering 316 (2017) 568–585.

[44] J. Deng, C. B. W. Pedersen, W. Chen, Connected morphable components-based multiscale topology optimization, Frontiers of Mechanical Engineering 14 (2) (2019) 129–140.

[45] W. Zhang, G. Dai, F. Wang, S. Sun, H. Bassir, Using strain energy-based prediction of effective elastic properties in topology optimization of material microstructures, Acta Mechanica Sinica 23 (1) (2007) 77–89.

[46] S. Duan, L. Xi, W. Wen, D. Fang, Mechanical performance of topology-optimized 3D lattice materials manufactured via selective laser sintering, Composite Structures 238 (2020).
URL https://doi.org/10.1016/j.compstruct.2020.111985

[47] G. Costa, M. Montemurro, J. Pailhès, A 2D topology optimisation algorithm in NURBS framework with geometric constraints, International Journal of Mechanics and Materials in Design 14 (4) (2018) 669–696.

[48] G. Costa, M. Montemurro, J. Pailhès, NURBS hyper-surfaces for 3D Topology Optimization problems, Mechanics of Advanced Materials and Structures (2019).
URL https://doi.org/10.1080/15376494.2019.1582826

[49] T. Rodriguez, M. Montemurro, P. L. Texier, J. Pailhès, Structural Displacement Requirement in a Topology Optimization Algorithm Based on Isogeometric Entities, Journal of Optimization Theory and Application 184 (2020) 250–276.

[50] G. Costa, M. Montemurro, Eigen-frequencies and harmonic responses in topology optimisation: A CAD-compatible algorithm, Engineering Structures 214 (2020) 110602.
URL https://doi.org/10.1016/j.engstruct.2020.110602

[51] G. Costa, M. Montemurro, J. Pailhès, Minimum length scale control in a NURBS-based SIMP method, Computer Methods in Applied Mechanics and Engineering 354 (2019) 963–989.

[52] G. Costa, M. Montemurro, J. Pailhès, N. Perry, Maximum length scale requirement in a topology optimisation method based on NURBS hyper-surfaces, CIRP Annals Manufacturing Technology 68 (2019) 153–156.

[53] L. Piegl, W. Tiller, The NURBS Book, Springer-Verlag, 2006.

[54] M. Delucia, A. Catapano, M. Montemurro, J. Pailhès, Determination of the effective thermoelastic properties of cork-based agglomerates, Journal of Reinforced Plastics and Composites 38 (16) (2019) 760–776.

[55] L. Cappelli, M. Montemurro, F. Dau, L. Guillaumat, Multi-scale identification of the viscoelastic behaviour of composite materials through a non-destructive test, Mechanics of Materials (2019).
URL https://doi.org/10.1016/j.mechmat.2019.103137

[56] E. J. Barbero, Finite Element Analysis of Composite Materials Using ANSYS®, CRC Press, 2013.

[57] R. M. Errico, What Is an Adjoint Model?, Bulletin of the American Meteorological Society 78 (11) (1997) 2577–2592.

[58] K. Svanberg, The Method of Moving Asymptotes – A new method for structural optimization, International Journal for Numerical Methods in Engineering 24 (1987) 359–373.